Development of explicit formulations of G45-based gas kinetic scheme for simulation of continuum and rarefied flows

Z. J. Liu [1,2] C. Shu,[1,*] S. Y. Chen,[2,†] W. Liu [1] Z. Y. Yuan [1] and L. M. Yang [3]

[1]*Department of Mechanical Engineering, National University of Singapore, 10 Kent Ridge Crescent, Singapore 119260*
[2]*Department of Mechanics and Aerospace Engineering, Southern University of Science and Technology, Shenzhen 518055, China*
[3]*Department of Aerodynamics, College of Aerospace Engineering,*
Nanjing University of Aeronautics and Astronautics, Yudao Street, Nanjing 210016, Jiangsu, China

In this work, the explicit formulations of the Grad's distribution function for the 45 moments (G45)-based gas kinetic scheme (GKS) are presented. Similar to the G13 function-based gas kinetic scheme (G13-GKS), G45-GKS simulates flows from the continuum regime to the rarefied regime by solving the macroscopic governing equations based on the conservation laws, which are widely used in conventional Navier-Stokes solver. These macroscopic governing equations are discretized by the finite volume method, where the numerical fluxes are evaluated by the local solution to the Boltzmann equation. The initial distribution function is reconstructed by the G45 distribution function, which is a higher order truncation of the Hermite expansion of distribution function compared with the G13 distribution function. Such high order truncation of Hermite expansion helps the present solver to achieve a better accuracy than G13-GKS. Moreover, the reconstruction of distribution function makes the development of explicit formulations of numerical fluxes feasible, and the evolution of the distribution function, which is the main reason why the discrete velocity method is expensive, is avoided. Several numerical experiments are performed to examine the accuracy of G45-GKS. Results show that the accuracy of the present solver for almost all flow problems is much better than G13-GKS. Moreover, some typical rarefied effects, such as the direction of heat flux without temperature gradients and thermal creep flow, can be well captured by the present solver.

I. INTRODUCTION

In recent years, the Boltzmann equation has been widely used to simulate multiscale flow problems which cover both the continuum and rarefied flow regimes. Since the Boltzmann equation is free from the continuum assumption, some ubiquitous rarefied effects, such as the direction of heat flux without temperature gradients [1–3], thermal creep [4–6], Knudsen paradox [7,8], and non-Newtonian behavior of shear stress [9–11], can be well addressed. However, solving the Boltzmann equation accurately and efficiently remains a challenging problem. Till now, several strategies in the microscopic level, the mesoscopic level, and the macroscopic level have been developed to achieve this goal. For example, the direct simulation Monte Carlo (DSMC) [12–14] method solves the Boltzmann equation by tracing the free transport and collision of simulation particles in the microscopic level. It is efficient and accurate for highly rarefied and hypersonic flow problems. However, its computational cost is enormous for continuum and near-continuum flows, and it suffers from statistical error for these flow problems. The discrete velocity method (DVM) [15–17] is developed in the mesoscopic level, and it solves the Boltzmann equation by evolving the gas distribution function in both the physical and velocity spaces. Therefore, the real gas distribution function can be addressed. Due to this feature, the DVM can simulate flows in all flow regimes accurately, but this feature also leads to a large amount of computational cost. Apart from the DSMC method and the DVM, the moment method [18–21] solves the Boltzmann equation by the macroscopic model. Compared with the DSMC method and the DVM, the moment method is efficient, and it has received a great success in different kinds of multiscale flow problems [22–27]. In order to address rarefied effects, a large number of high order moments are involved in the moment method, which makes the governing equations very complicated. Combining some good features of the DVM and the moment method, a Grad's distribution function-based gas kinetic scheme [28] to simulate flows in both the continuum and rarefied regimes was proposed in our previous work, and the explicit formulations were developed for Grad's distribution function for the 13 moments-based gas kinetic scheme (G13-GKS) [29]. In this work, we will further develop this solver to improve its accuracy. But first, the DVM and moment method will be introduced.

The DVM [15–17] solves the Boltzmann equation by tracing the distribution function in both the physical space and particle velocity space. That is, the particle velocity space is discretized, and the discrete velocity Boltzmann equation (DVBE) is solved. If the number of discrete velocities is large enough, the discrete distribution function can well address the

---

*Corresponding author: mpeshuc@nus.edu.sg
†Corresponding author: chensy@sustech.edu.cn

real gas distribution function, such that the flows in all flow regimes can be simulated accurately. Within the framework of the DVM, different algorithms have been developed to reconstruct the numerical fluxes. For example, the conventional DVM utilizes the upwind scheme to reconstruct the numerical fluxes [30–34]. However, such a simple approach is inefficient and inaccurate for flows in the continuum and near-continuum regime because the collisional effect is not considered when reconstructing the numerical fluxes. To overcome this drawback of the conventional DVM, an improved DVM was developed by Yang *et al.* [35]. The improved DVM also solves the macroscopic governing equations. In the solution process, the macroscopic governing equations predict the equilibrium distribution function, which enables the implementation of collisional effect when solving the DVBE. Apart from the conventional and improved DVM, the unified gas kinetic scheme (UGKS) [36–40] and the discrete unified gas kinetic scheme (DUGKS) [41,42] utilize the integral solution and characteristic solution of the Boltzmann equation to reconstruct the numerical fluxes, respectively. In these two methods, the collisional effect is considered when reconstructing the numerical fluxes, which makes them more accurate and efficient than the conventional DVM for flows in the continuum and near-continuum regime. Even though the DVM can simulate flows in all flow regimes accurately, the discretization in both the physical space and particle velocity space makes the DVM consume expensive computations and memory storages. To avoid the discretization in particle velocity space and further improve the efficiency in both the continuum and rarefied regimes, the method which only solves the problem in the physical space is desirable, and the moment method is such a method.

The moment method [18–21] derives the macroscopic equations of moments from the Boltzmann equation, in which the distribution function is first expanded by Hermite polynomials, and the Hermite expansion is truncated to a certain order. The coefficients of the Hermite expansion are determined by moment integrals of the distribution function. Next, the truncated Hermite expansion is substituted into the Boltzmann equation and the classical moment equations can be obtained. In 1949, Grad [19] truncated the Hermite expansion to the third order and derived the well-known 13 moment equations. Certainly, the Hermite expansion with a higher truncation order is closer to the real gas distribution function, such that the moment equations with large moment numbers can achieve a better accuracy. And the moment equations with large moment numbers are tested by many researchers [21,43,44]. At first, an algorithm to produce these equations was proposed by Weiss [43] and further developed by Struchtrup [21] and Au [44]. These equations have been tested for several one-dimensional problems, such as shock waves [44], light scattering [43,45], heat transfer [21], and sound propagation [43,45]. In the work of Weiss [43], 506 equations in a one-dimensional problem were computed, which corresponds to 15 180 moments in a three-dimensional case. The above mentioned moment equations are stable, but they cannot predict continuous shock wave with large Mach numbers due to their hyperbolic property. To overcome this shortcoming, the Chapman-Enskog type expansion and an order-of-magnitude approach were introduced into

the original moment equations, and the regularized moment equations were proposed [20,46]. Thanks to the regularization, the regularized moment equations are nonhyperbolic, and they retain the stability of original moment equations. The regularized moment equations are the most widely used moment equations in recent years, and they have received impressive success in several multiscale flow problems, such as Couette flow [26,27], Poiseuille flow [26,27], lid-driven cavity flow [23] and flow past a circular cylinder [24]. However, from the above analysis, we can see that the moment method usually uses a large number of governing equations, and the governing equations for high order moments are usually complicated, which limits the application of the moment method in some practical problems. Furthermore, adding higher order moments to achieve a better accuracy needs additional complicated moment equations. Therefore, developing a numerical scheme with the governing equations based on the conservation laws is attractive. The Grad's distribution function-based gas kinetic scheme [28] developed in our previous work is such a numerical scheme.

The Grad's distribution function-based gas kinetic scheme was developed within the framework of the gas kinetic scheme (GKS), which was proposed by Prendergast and Xu [47] and further developed by Chae *et al.* [48], Xu [49], and others [50,51]. GKS utilizes the finite volume method (FVM) to discretize the macroscopic governing equations. The numerical fluxes of the GKS are evaluated by the local solution to the Boltzmann equation, and the initial distribution function is reconstructed by first order Chapman-Enskog expansion. The GKS was further simplified by Shu and his co-workers, and the gas kinetic flux solver (GKFS) was proposed [52–58]. The computational cost of the GKFS is comparable to the conventional Navier-Stokes solver. However, limited by first order CE expansion, the GKS can only simulate flows in the continuum regime. To overcome this limitation, the Grad's distribution function was utilized to reconstruct the initial distribution function [28,29]. Thanks to such reconstruction, the Grad's distribution function-based gas kinetic scheme can give reasonable results for rarefied flows with moderate Knudsen numbers, and the evolution of the distribution function is avoided. In addition, this reconstruction makes the explicit formulations of numerical fluxes available, and the explicit formulations of Grad's distribution function for the 13 moments-based gas kinetic scheme (G13-GKS) were derived in our previous work [29]. Since the discretization in particle velocity space is not needed, the computational efficiency of the G13-GKS is much improved compared with DVM. Numerical experiments showed that the computational time needed for the G13-GKS is about 1% of the DVM and twice the Navier-Stokes solver for two-dimensional problems [29]. However, the G13-GKS may not satisfy the requirement of accuracy under some circumstances with large Knudsen number. Inspired by the moment method, the accuracy can be improved by using additional high order moments to describe the flows [21,43–45]. That is, replacing the G13 distribution function by the Grad's distribution function with 45 moments (G45). However, introducing higher order moments and determining them is not so easy and straightforward. The difficulty for treating G13 and G45 is not the same level. In the moment method, if we want to utilize more moments to describe

the nonequilibrium flows, additional moment equations are needed. The moment equations for high order moments are very complicated, and solving these equations is tedious work. A main contribution of the present work is that a simple and efficient way is utilized to determine the high order moments, which is an iteration process. That is, the high order moments at the cell interfaces are calculated by moment integrals, then their values at cell centers are calculated by the linear interpolation method. With the G45 distribution function reconstructed, the numerical fluxes of the G45 distribution function based-gas kinetic scheme (G45-GKS) can be calculated, and the explicit formulations of these numerical fluxes are first derived in this paper. In addition, the accuracy and efficiency of the G45-GKS are examined by several numerical examples. Numerical results show that the G45-GKS can achieve much better accuracy than the G13-GKS in most cases, especially for flows dominated by the variation of temperature. Although some high order moments are involved in the G45-GKS, the computational efficiency of the G45-GKS is still much higher than that of the DVM.

II. METHODOLOGY

A. Boltzmann equation and macroscopic governing equations

The macroscopic governing equations in this work are derived from the Boltzmann equation with the BGK collision model [59], which is written as

$$\frac{\partial f}{\partial t} + \xi_x \frac{\partial f}{\partial x} + \xi_y \frac{\partial f}{\partial y} = \frac{g-f}{\tau}, \tag{1}$$

where f is the phase state of gas and g is the equilibrium state. τ is the collisional time step, which means that the gas distribution function will approach its equilibrium state within τ. Both f and g are the functions of physical space $\boldsymbol{x} = (x, y)$, particle velocity space $\boldsymbol{\xi} = (\xi_x, \xi_y)$, phase energy ζ, and time t. Specifically, the equilibrium state is given as the Maxwellian distribution function:

$$g = \rho \left(\frac{\lambda}{\pi}\right)^{3/2} e^{-\lambda[(\xi_x-U)^2+(\xi_y-V)^2+\zeta^2]}, \tag{2}$$

where ρ and U, V are the density and macroscopic velocity components in the x and y direction, respectively. $\lambda = 1/(2RT)$, where R is the gas constant and T is the temperature. To obtain the macroscopic governing equations from Eq. (1), a vector of moments $\boldsymbol{\varphi}$ is introduced first, which is written as

$$\boldsymbol{\varphi} = \left(1, \xi_x, \xi_y, \tfrac{1}{2}\left(\xi_x^2 + \xi_y^2 + \zeta^2\right)\right)^T, \tag{3}$$

and the conservative variables can be connected to $\boldsymbol{\varphi}$ by the moment integrals of gas distribution function:

$$\boldsymbol{W} = (\rho, \rho U, \rho V, \rho E)^T = \int \boldsymbol{\varphi} f d\boldsymbol{\Xi}, \tag{4}$$

where $d\boldsymbol{\Xi} = d\xi_x d\xi_y d\zeta$ is the volume element in the particle velocity space. Then, multiplying the Boltzmann equation with $\boldsymbol{\varphi}$ and performing integration over the particle velocity

space we can get

$$\frac{\partial}{\partial t}\int \boldsymbol{\varphi} f d\boldsymbol{\Xi} + \frac{\partial}{\partial x}\int \xi_x \boldsymbol{\varphi} f d\boldsymbol{\Xi} + \frac{\partial}{\partial y}\int \xi_y \boldsymbol{\varphi} f d\boldsymbol{\Xi}$$
$$= \int \boldsymbol{\varphi}\frac{g-f}{\tau}d\boldsymbol{\Xi}. \tag{5}$$

According to the compatibility condition, the right-hand side of Eq. (5) is equal to $\boldsymbol{0}$. Therefore, Eq. (5) can be rewritten as

$$\frac{\partial \boldsymbol{W}}{\partial t} + \frac{\partial \boldsymbol{F}^x}{\partial x} + \frac{\partial \boldsymbol{F}^y}{\partial y} = \boldsymbol{0}, \tag{6}$$

where $\boldsymbol{F}^x$ and $\boldsymbol{F}^y$ are the fluxes in the x direction and y direction, and they are written as

$$\boldsymbol{F}^x = \left(F_1^x, F_2^x, F_3^x, F_4^x\right)^T = \int \xi_x \boldsymbol{\varphi} f d\boldsymbol{\Xi} \quad, \tag{7}$$

$$\boldsymbol{F}^y = \left(F_1^y, F_2^y, F_3^y, F_4^y\right)^T = \int \xi_y \boldsymbol{\varphi} f d\boldsymbol{\Xi}. \tag{8}$$

The macroscopic governing equations used in this work are shown in Eq. (6). They can be used to simulate flows in all flow regimes if and only if the distribution function f is accurately approximated. In order to solve the governing equations numerically, they are discretized by the finite volume method:

$$\frac{d\boldsymbol{W}}{dt} + \frac{1}{\Omega}\sum_{i=1}^{N_f} \boldsymbol{F}_i S_i = \boldsymbol{0}, \tag{9}$$

where N_f is the number of cell interface, Ω is the area of cell, $\boldsymbol{F}_i$ and S_i are the numerical fluxes at cell interface i and the length of cell interface i, respectively. Depending on the direction, the numerical fluxes $\boldsymbol{F}_i$ can be calculated by Eq. (7) or Eq. (8) with the distribution function f reconstructed at the cell interface. In the next section, the method to reconstruct the distribution function f at the cell interface will be introduced.

B. Reconstruction of distribution function at the cell interface

Similar to the G13-GKS [29], the distribution function f at the cell interface is calculated by the local solution to the Boltzmann equation. In this work, we might assume that the midpoint of the cell interface is located at the original point $(x = 0, y = 0)$ for simplicity, and the distribution function at the cell interface is written as

$$f(0, 0, t + \delta t) = \frac{\delta t}{\tau + \delta t}g(0, 0, t + \delta t)$$
$$+ \frac{\tau}{\tau + \delta t}f(-\xi_x \delta t, -\xi_y \delta t, t), \tag{10}$$

where $f(0, 0, t + \delta t)$ and $g(0, 0, t + \delta t)$ are the distribution function and equilibrium distribution function at the cell interface, and $f(-\xi_x \delta t, -\xi_y \delta t, t)$ is the distribution function at the surrounding point of cell interface. δt is the streaming time step. $g(0, 0, t + \delta t)$ can be reconstructed by the conservative variables at the cell interface at $t + \delta t$. These conservative variables can be calculated by $f(-\xi_x \delta t, -\xi_y \delta t, t)$ with the help of the compatibility condition, which will be introduced in the following subsection. Therefore, our task is to reconstruct $f(-\xi_x \delta t, -\xi_y \delta t, t)$ now. Similar to the G13-GKS,

$f(-\xi_x\delta t, -\xi_y\delta t, t)$ is approximated by the second order interpolation as

$$
f(-\xi_x\delta t, -\xi_y\delta t, t) = \begin{cases} f^l - \frac{\partial f^l}{\partial x}\xi_x\delta t - \frac{\partial f^l}{\partial y}\xi_y\delta t, & \xi_x > 0 \\ f^r - \frac{\partial f^r}{\partial x}\xi_x\delta t - \frac{\partial f^r}{\partial y}\xi_y\delta t, & \xi_x < 0 \end{cases},
$$

(11)

where f^l and f^r are the distribution functions at the left and right side of the cell interface. These distribution functions should be reconstructed appropriately to simulate flows in both the continuum regime and rarefied regime. In this work, these distribution functions are reconstructed by Grad's distribution function for 45 moments (G45), which is written as in Refs. [19,26,27]:

$$
f_{G45} = g\Bigg[1 + \frac{\sigma_{ij}C_iC_j}{2pRT} + \frac{C_iq_i}{pRT}\left(\frac{C^2}{5RT} - 1\right)
$$

$$
+ \frac{m_{ijk}C_iC_jC_k}{6p(RT)^2} + \frac{R_{ij}C_iC_j}{4p(RT)^2}\left(\frac{C^2}{7RT} - 1\right)
$$

$$
+ \frac{\Delta}{8pRT} \times \left(\frac{C^4}{15(RT)^2} - \frac{2C^2}{3RT} + 1\right)
$$

$$
+ \frac{\phi_{ijkl}C_iC_jC_kC_l}{24p(RT)^3} + \frac{\psi_{ijk}C_iC_jC_k}{12p(RT)^3}\left(\frac{C^2}{9RT} - 1\right)
$$

$$
+ \frac{C_i\Omega_i}{40p(RT)^2}\left(\frac{C^4}{7(RT)^2} - \frac{2C^2}{RT} + 5\right)\Bigg],
$$

(12)

where g is the Maxwellian distribution function given in Eq. (2), $C_i = \xi_i - u_i$ is the peculiar velocity in the i direction (u_i is the flow velocity in the i direction). p is the pressure. σ_{ij} are the stresses and q_i are the heat fluxes, while $m_{ijk}, R_{ij}, \Delta, \phi_{ijkl}, \psi_{ijk}, \Omega_i$ are the higher order moments. All these high order moments are defined by the moment integrals of distribution function as in Refs. [26,27]:

$$
\sigma_{ij} = \int C_{\langle i}C_{j\rangle}fd\Xi,
$$

(13)

$$
q_i = \int \frac{1}{2}C_iC^2fd\Xi,
$$

(14)

$$
m_{ijk} = \int C_{\langle i}C_jC_{k\rangle}fd\Xi,
$$

(15)

$$
R_{ij} = \int C_{\langle i}C_{j\rangle}C^2fd\Xi - 7RT\sigma_{ij},
$$

(16)

$$
\Delta = \int C^4fd\Xi - 15pRT,
$$

(17)

$$
\phi_{ijkl} = \int C_{\langle i}C_jC_kC_{l\rangle}fd\Xi,
$$

(18)

$$
\psi_{ijk} = \int C_{\langle i}C_jC_{k\rangle}C^2fd\Xi - 9RTm_{ijk},
$$

(19)

$$
\Omega_i = \int C_iC^4fd\Xi - 28RTq_i.
$$

(20)

In Eqs. (13)–(20), the angular brackets denote the trace free part of the symmetric tensor, and they are expressed by [27]

$$
C_{\langle i}C_{j\rangle} = C_iC_j - \frac{1}{3}\delta_{ij}C_kC_k,
$$

(21)

$$
C_{\langle i}C_jC_{k\rangle} = C_iC_jC_k - \frac{1}{5}(C_iC_rC_r\delta_{jk} + C_jC_rC_r\delta_{ik} + C_kC_rC_r\delta_{ij}),
$$

(22)

$$
C_{\langle i}C_jC_kC_{l\rangle} = C_iC_jC_kC_l - \frac{1}{7}(C_{\langle i}C_{j\rangle}C_rC_r\delta_{kl} + C_{\langle i}C_{k\rangle}C_rC_r\delta_{jl}
$$

$$
+ C_{\langle i}C_{l\rangle}C_rC_r\delta_{jk} + C_{\langle j}C_{k\rangle}C_rC_r\delta_{il} + C_{\langle j}C_{l\rangle}C_rC_r\delta_{ik}
$$

$$
+ C_{\langle k}C_{l\rangle}C_rC_r\delta_{ij}) - \frac{1}{15}(\delta_{ij}\delta_{kl}
$$

$$
+ \delta_{ik}\delta_{jl} + \delta_{il}\delta_{jk})C_rC_rC_sC_s.
$$

(23)

Once the distribution function at the cell interface is reconstructed, the numerical fluxes can be calculated by substituting $f(0, 0, t + \delta t)$ into Eqs. (7) and (8). In the next section, the basic formulations for the numerical fluxes in the x direction will be derived, while the basic formulations for the numerical fluxes in the y direction are given in Appendix C.

C. Basic formulation of numerical fluxes in the x direction

Substituting $f(0, 0, t + \delta t)$ into Eq. (7), we can get the numerical fluxes in the x direction as

$$
\boldsymbol{F}^x = \int \xi_x\boldsymbol{\varphi}\Bigg[\frac{\delta t}{\tau + \delta t}g(0, 0, t + \delta t)
$$

$$
+ \frac{\tau}{\tau + \delta t}f(-\xi_x\delta t, -\xi_y\delta t, t)\Bigg]d\Xi.
$$

(24)

For simple denotation, the $\boldsymbol{F}^x$ in Eq. (24) can be divided into two parts:

$$
\boldsymbol{F}^x = \frac{\delta t}{\tau + \delta t}\boldsymbol{F}^{x(0)} + \frac{\tau}{\tau + \delta t}\boldsymbol{F}^{x(1)},
$$

(25)

where

$$
\boldsymbol{F}^{x(0)} = \int \xi_x\boldsymbol{\varphi}g(0, 0, t + \delta t)d\Xi,
$$

(26)

$$
\boldsymbol{F}^{x(1)} = \int \xi_x\boldsymbol{\varphi}f(-\xi_x\delta t, -\xi_y\delta t, t)d\Xi.
$$

(27)

$\boldsymbol{F}^{x(0)}$ is contributed by the equilibrium distribution function at the cell interface, while $\boldsymbol{F}^{x(1)}$ is contributed by the distribution function at the surrounding points of cell interface. To calculate $\boldsymbol{F}^{x(0)}$, the conservative variables at the cell interface, which can be used to reconstruct the equilibrium distribution function, should be calculated first. According to the compatibility condition, the conservative variables can be calculated by the distribution function at the surrounding points of cell interface, which is written as in Ref. [29]:

$$
\boldsymbol{W} = \int \boldsymbol{\varphi}f(-\xi_x\delta t, -\xi_y\delta t, t)d\Xi.
$$

(28)

Substituting Eq. (11) into Eq. (28), we can get

$$
\boldsymbol{W} = \int_{\xi_x>0}\boldsymbol{\varphi}f^ld\Xi + \int_{\xi_x<0}\boldsymbol{\varphi}f^rd\Xi
$$

$$
- \delta t\frac{\partial}{\partial x}\left(\int_{\xi_x>0}\boldsymbol{\varphi}\xi_xf^ld\Xi + \int_{\xi_x<0}\boldsymbol{\varphi}\xi_xf^rd\Xi\right)
$$

$$
- \delta t\frac{\partial}{\partial y}\left(\int_{\xi_x>0}\boldsymbol{\varphi}\xi_yf^ld\Xi + \int_{\xi_x<0}\boldsymbol{\varphi}\xi_yf^rd\Xi\right),
$$

(29)

and the numerical fluxes $\boldsymbol{F}^{x(0)}$ can be given based on the variables calculated in Eq. (29):

$$
\boldsymbol{F}^{x(0)} = \int \boldsymbol{\varphi} g(0,0,t+\delta t) d\boldsymbol{\Xi} = \begin{pmatrix} \rho U \\ \rho U^2 + p \\ \rho UV \\ (\rho E + p)U \end{pmatrix}. \quad (30)
$$

Similar to Eq. (29), the numerical fluxes $\boldsymbol{F}^{x(1)}$ can be given by substituting Eq. (11) into Eq. (27), which is expressed as

$$
\begin{aligned}
\boldsymbol{F}^{x(1)} = {} & \int_{\xi_x>0} \xi_x \boldsymbol{\varphi} f^l d\boldsymbol{\Xi} + \int_{\xi_x<0} \xi_x \boldsymbol{\varphi} f^r d\boldsymbol{\Xi} \\
& - \delta t \frac{\partial}{\partial x}\left(\int_{\xi_x>0} \boldsymbol{\varphi} \xi_x \xi_x f^l d\boldsymbol{\Xi} + \int_{\xi_x<0} \boldsymbol{\varphi} \xi_x \xi_x f^r d\boldsymbol{\Xi} \right) \\
& - \delta t \frac{\partial}{\partial y}\left(\int_{\xi_x>0} \boldsymbol{\varphi} \xi_x \xi_y f^l d\boldsymbol{\Xi} + \int_{\xi_x<0} \boldsymbol{\varphi} \xi_x \xi_y f^r d\boldsymbol{\Xi} \right).
\end{aligned}
$$
$$(31)$$

Now our task is to present the explicit formulations of Eq. (29) and Eq. (31). Looking at these formulations in detail, we can see that they are composed of two types of moment integrals: $\int_{\xi_x>0} \xi_x^i \xi_y^j \zeta^k f^l d\boldsymbol{\Xi}$ and $\int_{\xi_x<0} \xi_x^i \xi_y^j \zeta^k f^r d\boldsymbol{\Xi}$, where $i, j, k = 0, 1, 2, \ldots$. In the following of this section, the moment integrals of G45 distribution function are denoted as in Ref. [60]:

$$
\begin{aligned}
\rho \langle \ldots \rangle_{>0} &= \int_{\xi_x>0} (\ldots) f_{G45} d\boldsymbol{\Xi} \\
\rho \langle \ldots \rangle_{<0} &= \int_{\xi_x<0} (\ldots) f_{G45} d\boldsymbol{\Xi}.
\end{aligned}
$$
$$(32)$$

Therefore, Eqs. (29) and (31) can be given explicitly by $\langle \xi_x^i \xi_y^j \zeta^k \rangle_{>0}$ and $\langle \xi_x^i \xi_y^j \zeta^k \rangle_{<0}$ with their derivatives. Then we need to derive the explicit formulations of $\langle \xi_x^i \xi_y^j \zeta^k \rangle_{>0}$ and $\langle \xi_x^i \xi_y^j \zeta^k \rangle_{<0}$. Because the G45 distribution function is a Maxwellian distribution function multiplying a polynomial of C_x, C_y, and ζ, it is easier to get $\langle \xi_x^i C_y^j \zeta^k \rangle_{>0}$ and $\langle \xi_x^i C_y^j \zeta^k \rangle_{<0}$ first, and then use them to calculate $\langle \xi_x^i \xi_y^j \zeta^k \rangle_{>0}$ and $\langle \xi_x^i \xi_y^j \zeta^k \rangle_{<0}$. To calculate $\langle \xi_x^i C_y^j \zeta^k \rangle_{>0}$ and $\langle \xi_x^i C_y^j \zeta^k \rangle_{<0}$, the moment integrals of Maxwellian distribution function are needed. Here, we denote the moment integrals of Maxwellian distribution function as

$$
\begin{aligned}
\rho \langle \ldots \rangle^e &= \int (\ldots) g d\boldsymbol{\Xi} \quad \rho \langle \ldots \rangle_{>0}^e = \int_{\xi_x>0} (\ldots) g d\boldsymbol{\Xi} \\
\rho \langle \ldots \rangle_{<0}^e &= \int_{\xi_x<0} (\ldots) g d\boldsymbol{\Xi},
\end{aligned}
$$
$$(33)$$

where "e" means that they are moment integrals of equilibrium distribution function. Then we have

$$
\begin{aligned}
\langle C_x^n \rangle^e &= \langle C_y^n \rangle^e = \langle \zeta^n \rangle^e \\
&= \begin{cases} 1, & n=0 \\ 0, & n=2k-1, k=1,2,3,\ldots \\ (2k-1)!!/(2^k \lambda^k), & n=2k, k=1,2,3,\ldots \end{cases}
\end{aligned}
$$
$$(34)$$

and

$$
\langle \xi_x^0 \rangle_{>0}^e = \frac{1}{2}[1 + \mathrm{erf}(\sqrt{\lambda^l} U^l)],
$$

$$
\langle \xi_x^1 \rangle_{>0}^e = U^l \langle \xi_x^0 \rangle_{>0}^e + \frac{1}{2} \frac{e^{-\lambda^l (U^l)^2}}{\sqrt{\lambda^l \pi}},
$$

$$
\langle \xi_x^{k+2} \rangle_{>0}^e = U^l \langle \xi_x^{k+1} \rangle_{>0}^e + \frac{k+1}{2\lambda^l} \langle \xi_x^k \rangle_{>0}^e, \ k=0,1,2,\ldots, \quad (35)
$$

$$
\langle \xi_x^0 \rangle_{<0}^e = \frac{1}{2} \mathrm{erfc}(\sqrt{\lambda^r} U^r),
$$

$$
\langle \xi_x^1 \rangle_{<0}^e = U^r \langle \xi_x^0 \rangle_{<0}^e - \frac{1}{2} \frac{e^{-\lambda^r (U^r)^2}}{\sqrt{\lambda^r \pi}},
$$

$$
\langle \xi_x^{k+2} \rangle_{<0}^e = U^r \langle \xi_x^{k+1} \rangle_{<0}^e + \frac{k+1}{2\lambda^r} \langle \xi_x^k \rangle_{<0}^e, \ k=0,1,2,\ldots \quad (36)
$$

With the help of the moment integrals given in Eqs. (34)–(36), the moment integrals $\langle \xi_x^i C_x^n C_y^j \zeta^k \rangle_{>0}^e$ can be expressed as

$$
\langle \xi_x^i C_x^n C_y^j \zeta^k \rangle_{>0}^e = \langle \xi_x^i C_x^n \rangle_{>0}^e \langle C_y^j \rangle^e \langle \zeta^k \rangle^e, \quad (37)
$$

where

$$
\langle \xi_x^i C_x^n \rangle_{>0}^e = (-1)^{n-m} \sum_{m=0}^n \frac{n!}{m!(n-m)!} \langle \xi_x^{m+i} \rangle_{>0}^e (U^l)^{n-m}. \quad (38)
$$

Next, $\langle \xi_x^i C_y^j \zeta^k \rangle_{>0}$ can be given with the help of $\langle \xi_x^i C_x^n C_y^j \zeta^k \rangle_{>0}^e$. For simple denotation, we define a function $\Phi(\sigma)$, which is written as

$$
\begin{aligned}
\Phi(\sigma) = {} & \frac{\sigma_{xx}}{2pRT} \langle \xi_x^i C_x^2 C_y^j \zeta^k \rangle_{>0}^e + 2\frac{\sigma_{xy}}{2pRT} \langle \xi_x^i C_x^1 C_y^{j+1} \zeta^k \rangle_{>0}^e \\
& + \frac{\sigma_{yy}}{2pRT} \langle \xi_x^i C_x^0 C_y^{j+2} \zeta^k \rangle_{>0}^e \\
& - \left(\frac{\sigma_{xx}}{2pRT} + \frac{\sigma_{yy}}{2pRT} \right) \langle \xi_x^i C_x^0 C_y^j \zeta^{k+2} \rangle_{>0}^e.
\end{aligned}
$$
$$(39)$$

The function Φ for other high order moments, such as $\Phi(q)$ and $\Phi(m)$, is shown in Appendix A. Now we can get the moment integral $\langle \xi_x^i C_y^j \zeta^k \rangle_{>0}$ as

$$
\begin{aligned}
\langle \xi_x^i C_y^j \zeta^k \rangle_{>0} = {} & \langle \xi_x^i C_x^0 C_y^j \zeta^k \rangle_{>0}^e + \Phi(\sigma) + \Phi(q) + \Phi(m) \\
& + \Phi(R) + \Phi(\Delta) + \Phi(\phi) + \Phi(\psi) + \Phi(\Omega).
\end{aligned}
$$
$$(40)$$

Next, $\langle \xi_x^i \xi_y^j \zeta^k \rangle_{>0}$ can be calculated by $\langle \xi_x^i C_y^j \zeta^k \rangle_{>0}$ using binomial theory:

$$
\langle \xi_x^i \xi_y^j \zeta^k \rangle_{>0} = \sum_{m=0}^j \frac{j!}{m!(j-m)!} \langle \xi_x^i C_y^m \zeta^k \rangle_{>0} (V^l)^{j-m}. \quad (41)
$$

$\langle \xi_x^i \xi_y^j \zeta^k \rangle_{<0}$ can be calculated using a similar method with the integrations conducted at the right side of cell interface. Based on $\langle \xi_x^i \xi_y^j \zeta^k \rangle_{>0}$ and $\langle \xi_x^i \xi_y^j \zeta^k \rangle_{<0}$, we can define a set of parameters M_{ijk} as

$$
M_{ijk} = \int \xi_x^i \xi_y^j \zeta^k f(-\xi_x \delta t, -\xi_y \delta t, t) d\boldsymbol{\Xi}, \quad (42)
$$

and M_{ijk} can be expressed as

$$
\begin{aligned}
M_{ijk} = {}& \rho^l \langle \xi_x^i \xi_y^j \zeta^k \rangle_{>0} + \rho^r \langle \xi_x^i \xi_y^j \zeta^k \rangle_{<0} \\
& - \delta t \frac{\partial}{\partial x} \left(\rho^l \langle \xi_x^{i+1} \xi_y^j \zeta^k \rangle_{>0} + \rho^r \langle \xi_x^{i+1} \xi_y^j \zeta^k \rangle_{<0} \right) \\
& - \delta t \frac{\partial}{\partial y} \left(\rho^l \langle \xi_x^i \xi_y^{j+1} \zeta^k \rangle_{>0} + \rho^r \langle \xi_x^i \xi_y^{j+1} \zeta^k \rangle_{<0} \right), \quad (43)
\end{aligned}
$$

where the derivatives in Eq. (43) are calculated by the central difference scheme. With the help of M_{ijk}, the conservative variables at the cell interface can be expressed by

$$
\rho = M_{000}, \quad (44)
$$

$$
\rho U = M_{100}, \quad (45)
$$

$$
\rho V = M_{010}, \quad (46)
$$

$$
\rho E = \tfrac{1}{2}(M_{200} + M_{020} + M_{002}). \quad (47)
$$

Subsequently, the numerical fluxes $\boldsymbol{F}^{x(0)}$ can be given by Eq. (30) using the conservative variables calculated from Eqs. (44)–(47), and we can also get the numerical fluxes $\boldsymbol{F}^{x(1)}$ by

$$
F_\rho^{x(1)} = M_{100}, \quad (48)
$$

$$
F_{\rho U}^{x(1)} = M_{200}, \quad (49)
$$

$$
F_{\rho V}^{x(1)} = M_{110}, \quad (50)
$$

$$
F_{\rho E}^{x(1)} = \tfrac{1}{2}(M_{300} + M_{120} + M_{102}). \quad (51)
$$

D. Basic formulations for high order moments

After computing the numerical fluxes, the stresses, heat fluxes, and other high order moments should also be updated to reconstruct the distribution function at the surrounding points of cell interface for the next time step. In the moment method [46], these high order moments are determined by solving complicated differential equations, which makes the solution process of the moment method very tedious. In this work, according to the definition of these high order moments, they are calculated directly by the moment integrals of distribution function, which is inspired from DVM [17]. Thanks to this strategy, the solution process to determine these high order moments is simple and straightforward.

For example, the shear stresses at the cell interface can be expressed by substituting Eq. (10) into Eq. (13):

$$
\begin{aligned}
\sigma_{xx} &= \int \left(C_x C_x - \frac{1}{3}\left(C_x^2 + C_y^2 + \zeta^2\right) \right) \left[\frac{\delta t}{\tau + \delta t} g(0,0,t+\delta t) + \frac{\tau}{\tau + \delta t} f(-\xi_x \delta t, -\xi_y \delta t, t) \right] d\boldsymbol{\Xi}, \\
\sigma_{xy} &= \int C_x C_y \left[\frac{\delta t}{\tau + \delta t} g(0,0,t+\delta t) + \frac{\tau}{\tau + \delta t} f(-\xi_x \delta t, -\xi_y \delta t, t) \right] d\boldsymbol{\Xi}, \\
\sigma_{yy} &= \int \left(C_y C_y - \frac{1}{3}\left(C_x^2 + C_y^2 + \zeta^2\right) \right) \left[\frac{\delta t}{\tau + \delta t} g(0,0,t+\delta t) + \frac{\tau}{\tau + \delta t} f(-\xi_x \delta t, -\xi_y \delta t, t) \right] d\boldsymbol{\Xi}.
\end{aligned} \quad (52)
$$

Similarly, the heat fluxes at the cell interface can be expressed by substituting Eq. (10) into Eq. (14):

$$
\begin{aligned}
q_x &= \frac{1}{2} \int C_x C^2 \left[\frac{\delta t}{\tau + \delta t} g(0,0,t+\delta t) + \frac{\tau}{\tau + \delta t} f(-\xi_x \delta t, -\xi_y \delta t, t) \right] d\boldsymbol{\Xi}, \\
q_y &= \frac{1}{2} \int C_y C^2 \left[\frac{\delta t}{\tau + \delta t} g(0,0,t+\delta t) + \frac{\tau}{\tau + \delta t} f(-\xi_x \delta t, -\xi_y \delta t, t) \right] d\boldsymbol{\Xi}.
\end{aligned} \quad (53)
$$

To get the explicit formulations of the high order moments, a new set of parameters Λ_{ijk} is introduced first:

$$
\Lambda_{ijk} = \frac{\tau}{\tau + \delta t} \int C_x^i C_y^j \zeta^k f(-\xi_x \delta t, -\xi_y \delta t, t + \delta t) d\boldsymbol{\Xi}. \quad (54)
$$

Λ_{ijk} can be given with the help of M_{ijk} and the binomial theory as

$$
\Lambda_{ijk} = \frac{\tau}{\tau + \delta t} \sum_{n=1}^{i} \sum_{m=1}^{j} (-1)^{n+m} \frac{i!}{(i-n)!n!} \frac{j!}{(j-m)!m!} M_{nmk} U^n V^m. \quad (55)
$$

With the help of Λ_{ijk}, the stresses given by Eq. (52) can be expressed as

$$
\begin{aligned}
\sigma_{xx} &= \tfrac{1}{3}(2\Lambda_{200} - \Lambda_{020} - \Lambda_{002}), \\
\sigma_{xy} &= \Lambda_{110}, \\
\sigma_{yy} &= \tfrac{1}{3}(2\Lambda_{020} - \Lambda_{200} - \Lambda_{002}).
\end{aligned} \quad (56)
$$

In the same way, the heat fluxes given by Eq. (53) can be expressed as

$$
\begin{aligned}
q_x &= \tfrac{1}{2}(\Lambda_{300} + \Lambda_{120} + \Lambda_{102}), \\
q_y &= \tfrac{1}{2}(\Lambda_{210} + \Lambda_{030} + \Lambda_{012}).
\end{aligned} \quad (57)
$$

For other high order moments, they can also be calculated by Λ_{ijk}, and their formulations are shown in Appendix B. Note that the above high order moments are calculated at the

cell interface. Once they are available, we can use them to update their values at the cell center through interpolation. For uniform Cartesian mesh, their values at the cell center can be taken as the average values of cell interface, which is the same as the G13-GKS [29].

E. Implementation of boundary condition

In order to simulate flows in both the continuum regime and rarefied regime, the Maxwellian boundary condition with the isothermal wall is implemented in the present solver. This boundary condition is also used in the DVM [17] and the G13-GKS [29]. Under this boundary condition, the gas particles collide with the wall and reflect back with a Maxwellian distribution function, which is written as

$$f_R(0,0,t) = \rho_W \left(\frac{1}{2\pi RT_W} \right)^{3/2} e^{-[(\xi_x - U_W)^2 + (\xi_y - V_W)^2 + \zeta^2 / 2RT_W]},$$
(58)

where $f_R(0,0,t)$ is the distribution function of reflecting particles at the wall ($x=0, y=0$). The temperature T_W and macroscopic velocities U_W, V_W of this distribution function are determined by the wall. The density ρ_W should be determined specifically to guarantee that no particle penetrates the wall.

Here, the left boundary is taken as an example, and the density ρ_W is determined by

$$\rho_W = -\frac{\int_{\xi_x < 0} \xi_x f(-\xi_x \delta t, -\xi_y \delta t, t) d\Xi}{\left(\frac{1}{2\pi RT_W} \right)^{3/2} \int_{\xi_x > 0} \xi_x e^{-1/2RT_W \left[(\xi_x - U)^2 + (\xi_y - V)^2 + \zeta^2 \right]} d\Xi}.$$
(59)

With the help of M_{ijk}, ρ_W can be given by

$$\rho_W = -\frac{M_{100}^r - \frac{\partial M_{200}^r}{\partial x} - \frac{\partial M_{110}^r}{\partial y}}{\frac{U_W}{2}[1 + \mathrm{erf}(\sqrt{\lambda_W} U_W)] + \frac{1}{2} \frac{\exp(-\lambda_W U_W^2)}{\sqrt{\lambda_W \pi}}}.$$
(60)

Till now, the distribution function of the reflecting gas particles is determined. And the distribution function of gas particles at the internal interface is still reconstructed by the G45 distribution function. Using these distribution functions, the numerical fluxes and high order moments at the left wall can be calculated. Similarly, the numerical fluxes and high order moments at other boundaries can also be calculated.

F. Determination of collision time and streaming time step

Now looking back to Eq. (25), there are still two parameters, the relaxation time τ and streaming time step δt, which need to be determined. The relaxation time τ is defined by

$$\tau = \frac{\mu}{p},$$
(61)

where μ is the dynamic viscosity, which is determined by different collision models, such as the hard sphere (HS) model and the variable hard sphere (VHS) model.

The streaming time step δt is related to the distribution function at the cell interface. And the principle to determine δt is that the free transport distance of the particle should be smaller than half of the cell size, which means

$$\xi_x \delta t \leqslant \tfrac{1}{2}\Delta x, \quad \xi_y \delta t \leqslant \tfrac{1}{2}\Delta y$$
(62)

Theoretically, the domain of particle velocity is $\xi_x, \xi_y \in (-\infty, \infty)$. However, the infinite value of ξ_x and ξ_y will lead to $\delta t \to 0$, which will eliminate the effect of the collisional term in the Boltzmann equation. To resolve this problem, a reference velocity U_{ref} is introduced to cut off the infinite domain of particle velocity, and the streaming time step is determined by

$$\delta t = \frac{\mathrm{Minimum}(\Delta x, \Delta y)}{2U_{\mathrm{ref}}}.$$
(63)

Under this situation, only the particles with velocity $\xi_x, \xi_y \in (-U_{\mathrm{ref}}, U_{\mathrm{ref}})$ are considered for the streaming process, and the particles with velocity beyond the above domain are ignored. Then, we should check whether particles ignored due to the cutting off have an effect on the results obtained. In fact, if U_{ref} is large enough, and the gas particles satisfy the Maxwellian distribution function, most of the particles are distributed within $\xi_x, \xi_y \in (-U_{\mathrm{ref}}, U_{\mathrm{ref}})$. For example, if U_{ref} is set as $\max(U, V) + 2.0\sqrt{2RT}$, over 99.0666% of the particles are in the domain of $\xi_x, \xi_y \in (-U_{\mathrm{ref}}, U_{\mathrm{ref}})$. And if U_{ref} is increased to $\max(U, V) + 2.5\sqrt{2RT}$, the above percentage is increased to 99.9186%. For flows in the continuum and transition regime, the values of high order moments are small, such that both the G13 and G45 distribution functions will not deviate from the Maxwellian distribution function much. Therefore, when U_{ref} is large enough, only a few particles are ignored for the streaming process when the initial distribution function is reconstructed by the G13 or G45 distribution function. The previous test based on the G13-GKS has demonstrated that when U_{ref} is large enough, it has almost no effect on the results obtained for both the continuum and rarefied regime [29]. Therefore, we need to set an adequate value of U_{ref} to guarantee that most particles are considered for the streaming process and the insufficient collisional effect is avoided. In the numerical experiments of this work, the U_{ref} is set as $5.0\sqrt{2RT_0}$ (T_0 is the temperature of the reference state).

G. Computational sequence

(1) Calculate the moment integrals of the G45 distribution function $\langle \xi_x^i \xi_y^j \zeta^k \rangle_{>0}$ and $\langle \xi_x^i \xi_y^j \zeta^k \rangle_{<0}$, and calculate their derivatives by the central difference scheme. Use $\langle \xi_x^i \xi_y^j \zeta^k \rangle_{>0}$ and $\langle \xi_x^i \xi_y^j \zeta^k \rangle_{<0}$ to calculate the parameters M_{ijk} by Eq. (43).

(2) With the help of M_{ijk}, calculate the conservative variables at the cell interface $\boldsymbol{W}$ using Eqs. (44)–(47). Then use $\boldsymbol{W}$ to calculate the numerical fluxes $\boldsymbol{F}_x^{(0)}$ by Eq. (30).

(3) With the help of M_{ijk}, calculate the numerical fluxes $\boldsymbol{F}_x^{(1)}$ by Eqs. (48)–(51).

(4) Determine the relaxation time τ by Eq. (61) and streaming time step δt by Eq. (63).

(5) Calculate the total numerical fluxes $\boldsymbol{F}_x$ by Eq. (25).

(6) Starting from M_{ijk}, calculate Λ_{ijk} by Eq. (55).

(7) With the help of Λ_{ijk}, calculate the high order moments at the cell interface using Eqs. (56) and (57). Then use the linear interpolation method to calculate the high order moments at the cell center.

(8) Use a similar way to calculate the numerical fluxes in the y direction.

(9) Solve the macroscopic governing Eq. (9) by the three-stage Runge-Kutta scheme.

(10) Repeat steps (1)–(9) until the converged solution is reached.

III. NUMERICAL EXAMPLES

In this section, some practical flow problems, such as flows arising from temperature discontinuity, thermal cavity flows induced by temperature gradients, thermal transpiration flow, and lid-driven cavity flow, are utilized to test the accuracy of the present solver. In addition, the ability of the present solver to capture some physical properties of rarefied flow, such as the direction of heat flux without temperature gradients and thermal creep, is also validated. For flows in the continuum regime, the results of the conventional Navier-Stokes solver [61] and the circular function-based gas kinetic scheme (CGKS) [53] are used as the benchmark data. For flows in the rarefied regime, the results of the DVM [17] are used as the benchmark data.

A. Case 1: Flows arising from temperature discontinuity

The first test case is the flows arising from temperature discontinuity. This test case was studied by regularized moment equations [22], the UGKS [39], the DVM [62], and the G13-GKS [29] before. The computational domain of this test case is a square cavity with length $L = 1$ m. The computational domain is divided uniformly into 60×60 cells, and the Gauss-Hermite quadrature with 28×28 mesh points is used for the DVM. The temperature of the bottom wall of this square cavity is set as $T_H = 2T_0 = 546$ K, while the temperature of other three walls is set as $T_C = T_0 = 273$ K. The Knudsen number is defined as

$$\text{Kn} = \lambda_0/L, \quad (64)$$

where λ_0 is the mean free path of particle at the reference state, and it is related to the dynamic viscosity μ_0 at the reference state by

$$\lambda_0 = \frac{4\alpha_0(5 - 2w_0)(7 - 2w_0)}{5(\alpha_0 + 1)(\alpha_0 + 2)\sqrt{2\pi RT_0}} \frac{\mu_0}{\rho_0}, \quad (65)$$

where ρ_0 is the density of the reference state. α_0 and w_0 are parameters of the intermolecular interaction models of the reference state. In this work, the HS model is used for the reference state, such that $\alpha_0 = 1$ and $w_0 = 0.5$. The dynamic viscosity μ is determined by

$$\mu = \mu_0 \left(\frac{T}{T_0}\right)^w, \quad (66)$$

where w is equal to 0.81 in this test case. To compare the accuracy and efficiency of the present solver with the G13-GKS, cases with Kn = 0.01, 0.075, 0.15, and 0.3 are tested.

The results obtained by the DVM [17], the G13-GKS, and the present solver with different Knudsen numbers are shown in Figs. 1–4. From Fig. 1, we can see that both the results of the G13-GKS and the present solver can match the DVM data well for Kn = 0.01. Next, the Knudsen number is increased to 0.075. We can see from Fig. 2 that the results predicted by the G13-GKS start to deviate from the DVM slightly, and
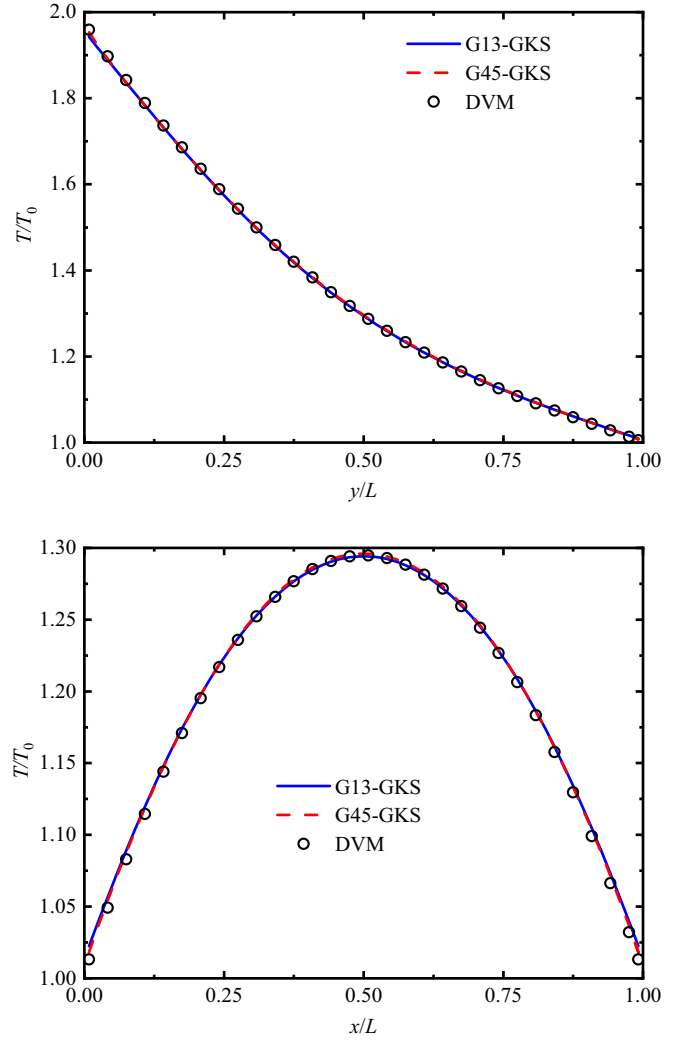
FIG. 1. Temperature along the vertical centerline (top) and horizontal centerline (bottom) of the cavity for Kn = 0.01.

the results predicted by the present solver can still match the DVM data very well. For Kn = 0.15, the deviation between the results of the G13-GKS and the DVM becomes larger compared with that for Kn = 0.075, but the results predicted by the G45-GKS can agree with the DVM data. When the Knudsen number is increased to 0.3, the G13-GKS cannot obtain accurate results. Nevertheless, the G45-GKS can also predict quite accurate results under this Knudsen number. Based on the above analysis, a primary conclusion can be made that the accuracy is improved apparently after using the G45 distribution function to initialize the distribution function at the surrounding points of the cell interface. And this primary conclusion can also be confirmed by the following numerical test cases.

Next, the convergence history of the G45-GKS is compared with that of the G13-GKS in Fig. 5. As shown in Fig. 5, the residual of the G45-GKS decreases quickly for all Knudsen numbers, and this decrease is quicker for a larger Knudsen number. Such quick convergence indicates that the stability of the G45-GKS is pretty good. Also, we can see that the convergence history of the G45-GKS is very close to the G13-GKS.
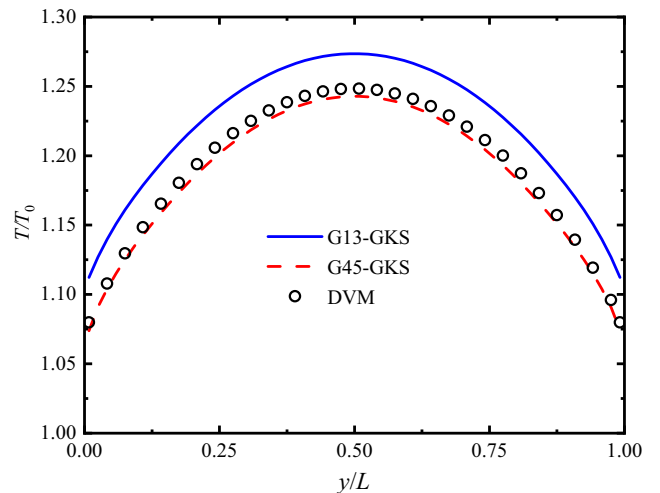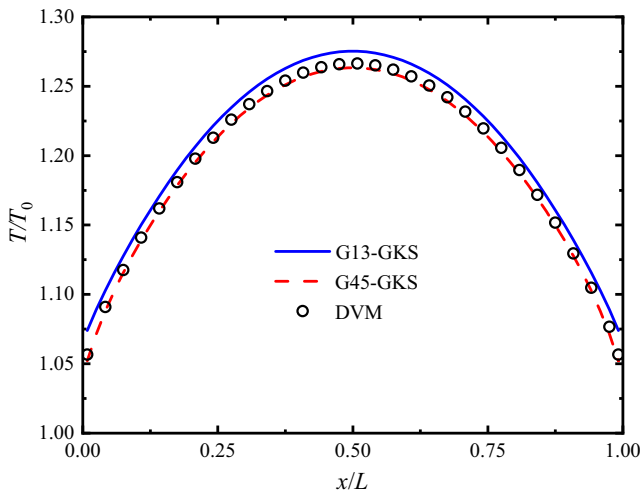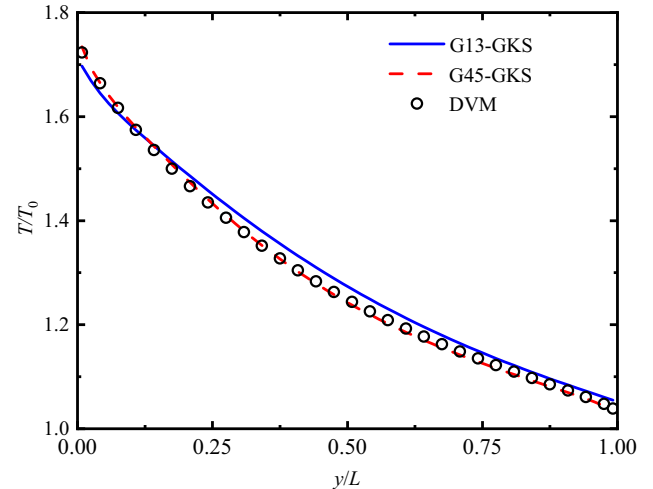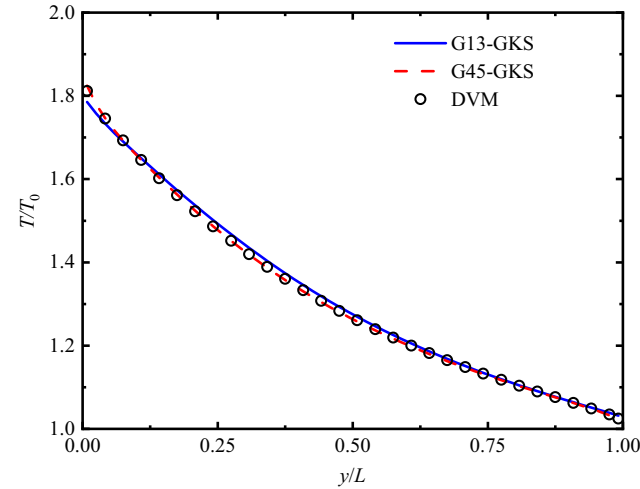
FIG. 2. Temperature along the vertical centerline (top) and horizontal centerline (bottom) of the cavity for Kn = 0.075.

FIG. 3. Temperature along the vertical centerline (top) and horizontal centerline (bottom) of the cavity for Kn = 0.15.

The reason for this phenomenon was indicated in the moment method [19,46]. That is, the values of high order moments are usually much smaller than those of low order moments. It is the low order moments that dominate the results obtained, while the high order moments mainly make corrections on the results. In addition, we compare the computational efficiency of the G13-GKS and G45-GKS. For Kn = 0.001, the G13-GKS uses 188.42 s to get the converged results, while the G45-GKS uses 764.99 s. For Kn = 0.075, the G13-GKS uses 64.17 s to get the converged results, while the G45-GKS uses 278.73 s. For Kn = 0.15, the computational time for the G13-GKS is 45.58 s, while this time for the G45-GKS is 215.94 s. When Kn is increased to 0.3, the computational time for the G13-GKS is 48.41 s, while this time for the G45-GKS is 192.08 s. From the above test, we can see that the G45-GKS uses about four times the computational time of the G13-GKS to get converged results. The reason is that more high order moments are needed to calculate in the G45-GKS, and the G45 distribution function is more complicated than the G13 distribution function. Nevertheless, since the computational time needed for the G13-GKS is just about 1% of that for

the DVM [29], the computational efficiency of the G45-GKS is still much higher than for the DVM.

B. Case 2: Thermal cavity flows induced by temperature gradients at wall

The second test case is the flows arising from temperature gradients, and this test case was studied by Yang *et al.* [63] using the moment methods. The schematic diagram of this test case is shown in Fig. 6. For a cavity with length $L = 1$ m, the temperature at the left and right walls is kept as 263 K. At the top wall and bottom wall, the temperature T_f increases linearly from $T_C = 263$ K to $T_H = 283$ K in the left half of the domain and decreases linearly from $T_H = 283$ K to $T_C = 263$ K in the right half of the domain. The computational domain is divided uniformly into 60×60 cells, and the Gauss-Hermite quadrature with 28×28 mesh points is used for the DVM. In this test case, the Knudsen number is defined by Eq. (64) and the viscosity at the reference state is given by Eq. (65). And the real viscosity is given by Eq. (66) with the reference temperature given as $T_0 = 273$ K.
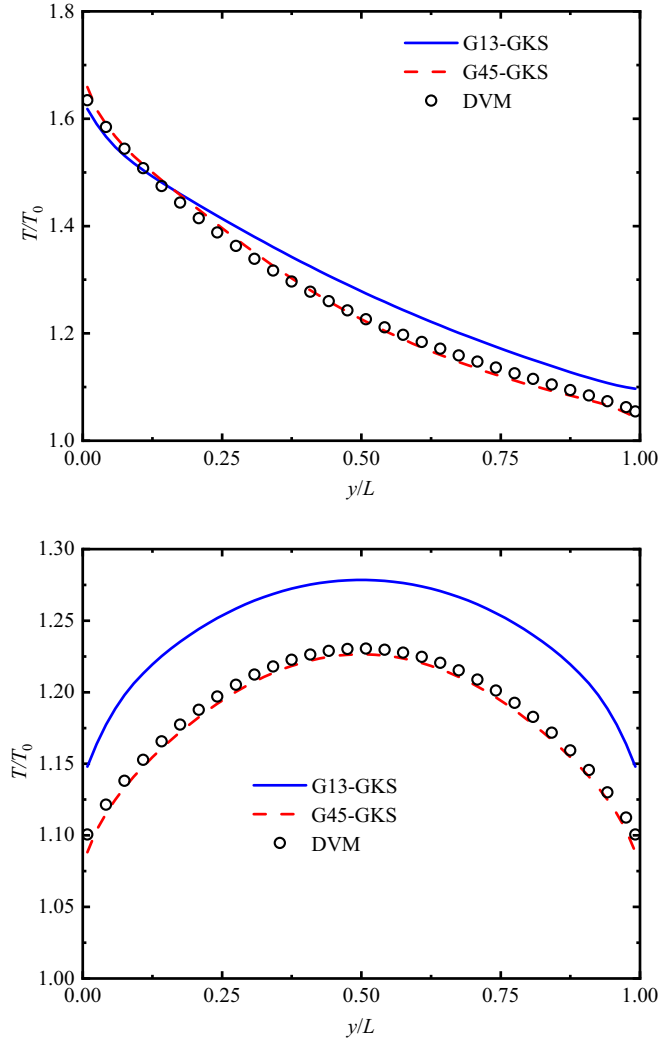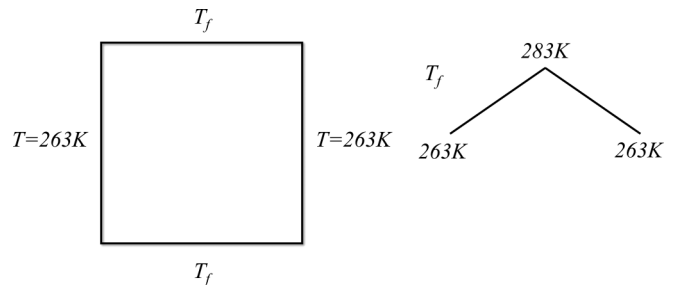
FIG. 4. Temperature along the vertical centerline (top) and horizontal centerline (bottom) of the cavity for Kn = 0.3.

Results of the DVM [17], the G13-GKS, and the G45-GKS with different Knudsen numbers (Kn = 0.01, 0.075, 0.15, and 0.3) are compared. These results are shown in Figs. 7–10. Similar to the last test case, both the G13-GKS and the G45-GKS can predict accurate results when Kn is equal to 0.01. When Kn is increased to 0.075, a little difference between the results of the DVM and G13-GKS appears, but the G45-GKS can also predict accurate results under this Knudsen number. After increasing Kn further to 0.15, the deviation between the results of the DVM and G13-GKS gets larger, but the results of the G45-GKS can still match the DVM data well. Next, the Knudsen number is increased to 0.3, which is quite large. Under this Knudsen number, the deviation between the results of the G13-GKS and the DVM is quite large. In addition, the results predicted by the G45-GKS cannot match the DVM data well. Nevertheless, the results predicted by the G45-GKS are much closer to the DVM data compared with those predicted by the G13-GKS. The results of the thermal cavity flows induced by temperature gradients help us to confirm that the G45-GKS can predict much more accurate results compared with the G13-GKS.
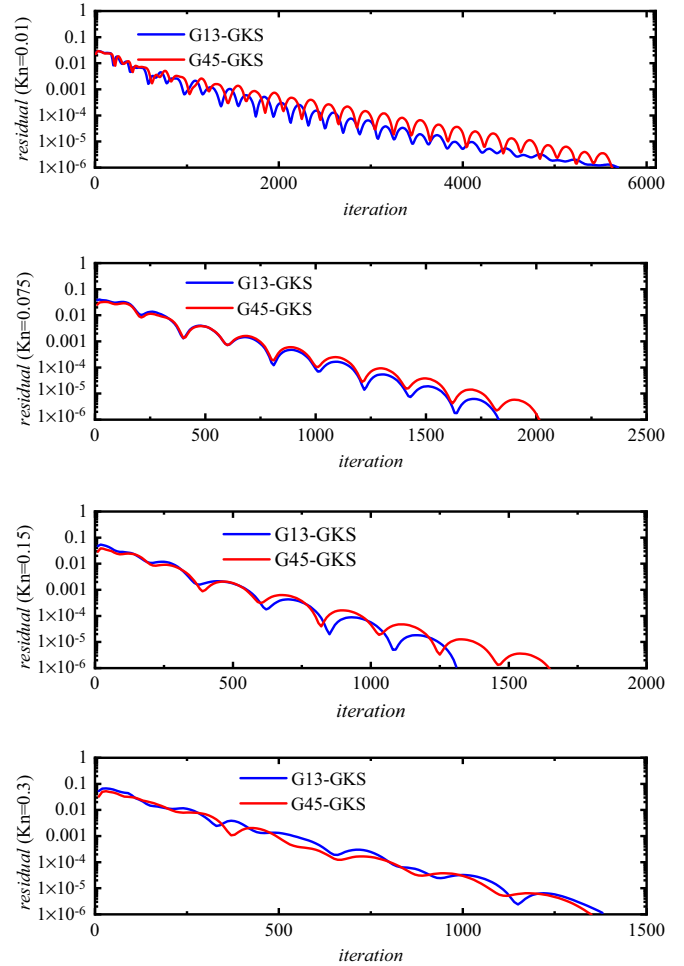
FIG. 5. Convergence history of flows arising from temperature discontinuity for Kn = 0.01, Kn = 0.075, Kn = 0.15, and Kn = 0.3.

C. Case 3: Lid-driven cavity flow

Next, the lid-driven cavity flow is simulated to examine the accuracy of the present solver for both the continuum and rarefied flow problems. This test case has been studied by John *et al.* [64,65] using the DSMC method, by Huang *et al.* [40] using the UGKS, by Rena *et al.* [23] using the moment method, and by Yang *et al.* [17] using the DVM. The computational domain of this test case is a cavity with length $L = 1$ m. The computational domain is divided uniformly into 60×60 cells, and the Gauss-Hermite quadrature with 28×28 mesh

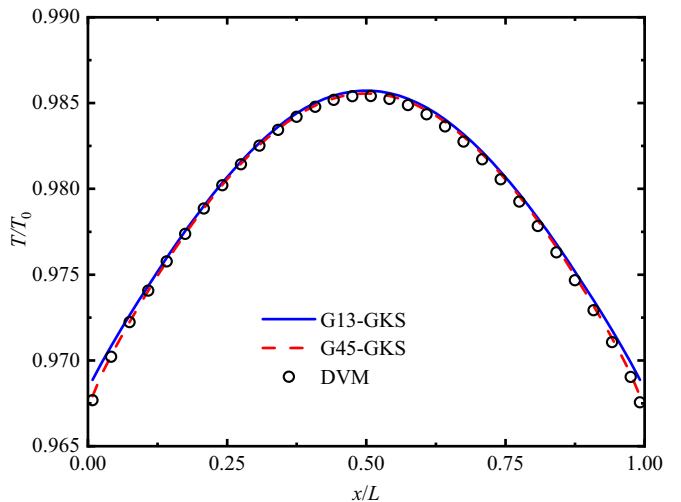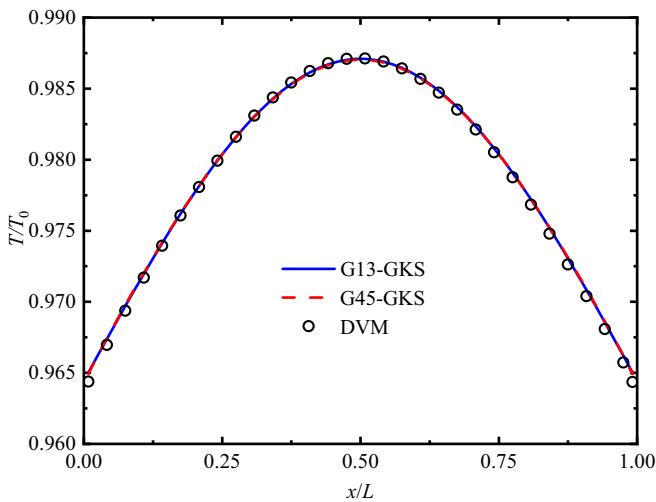FIG. 6. Schematic diagram of thermal cavity flows induced by temperature gradients at wall.
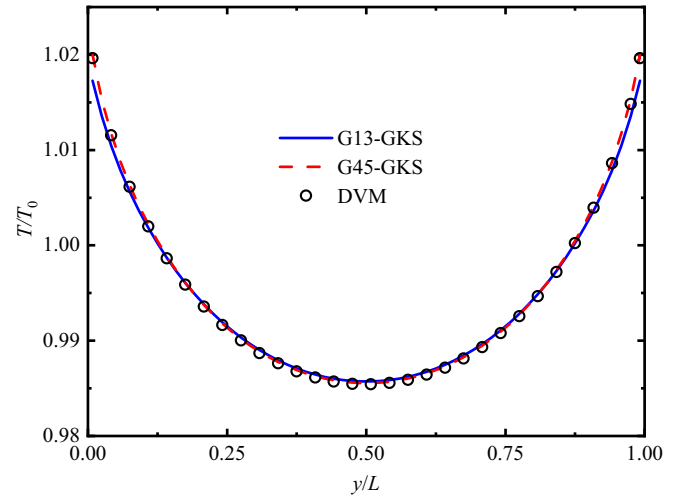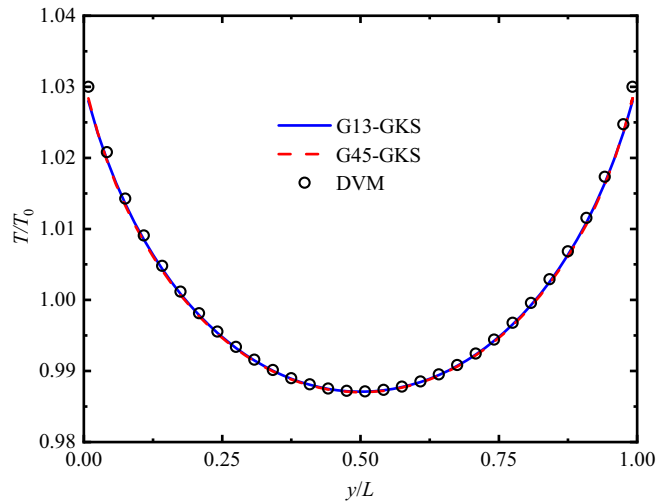
FIG. 7. Temperature along the vertical centerline (top) and horizontal centerline (bottom) of the cavity for Kn = 0.01.

FIG. 8. Temperature along the vertical centerline (top) and horizontal centerline (bottom) of the cavity for Kn = 0.075.

points is used for the DVM. The wall temperature is kept at $T_W = T_0 = 273$ K. The U velocity of the top wall is equal to $0.15\sqrt{2RT_0}$, and the other walls remain stationary. The reference viscosity μ_0 is determined by Eq. (65), and the real viscosity is given by Eq. (66).

At the beginning, the performance of the present solver for the rarefied flow problem is examined by comparing the results of the G13-GKS and G45-GKS with different Knudsen numbers. As shown in Figs. 11 and 12, when Kn = 0.01 and Kn = 0.075, both the results predicted by the G13-GKS and G45-GKS can match those of the DVM basically. When the Knudsen number is increased to 0.3, from Fig. 13, the results predicted by the G13-GKS and G45-GKS deviate from the DVM data. Nevertheless, we can see that the results predicted by the G45-GKS are more accurate than those predicted by the G13-GKS, which demonstrates that the G45-GKS can access rarefied flow problems with a larger Knudsen number.

For lid-driven cavity flow, a well-known rarefied effect is the direction of heat flux without temperature gradients. the DVM, the moment method, and the G13-GKS have demonstrated their ability to capture this important property [17,23,29]. Next, the temperature contour and corresponding

heat fluxes predicted by the present solver are plotted to show the ability of the present solver to capture this property. Results of Kn = 0.01 and Kn = 0.15 are shown in Figs. 14 and 15, respectively. When Kn = 0.01, both the G13-GKS and G45-GKS can predict reasonable temperature contour. And we can see that the heat fluxes predicted by the DVM, G13-GKS, and G45-GKS go from the upper left corner (low temperature region) to the upper right corner (high temperature region). In the rest regions of the cavity, the heat fluxes go from the high temperature region to the low temperature region as ordinary continuum flow since the nonequilibrium effect in these regions is weaker. Next, the Knudsen number is increased to 0.15, compared with the G13-GKS, the G45-GKS can predict a maximum temperature and a minimum temperature much closer to those of the DVM. In addition, from the heat flux shown in Fig. 15, the direction of heat flux without temperature gradients can be well captured by both the G13-GKS and G45-GKS.

After validating the present solver for flows in the rarefied regime, the accuracy of the present solver for flows in the continuum regime is then examined by computing the lid-driven cavity flow with Re = 100, 400, and 1000. And the results

FIG. 9. Temperature along the vertical centerline (top) and horizontal centerline (bottom) of the cavity for Kn = 0.15.
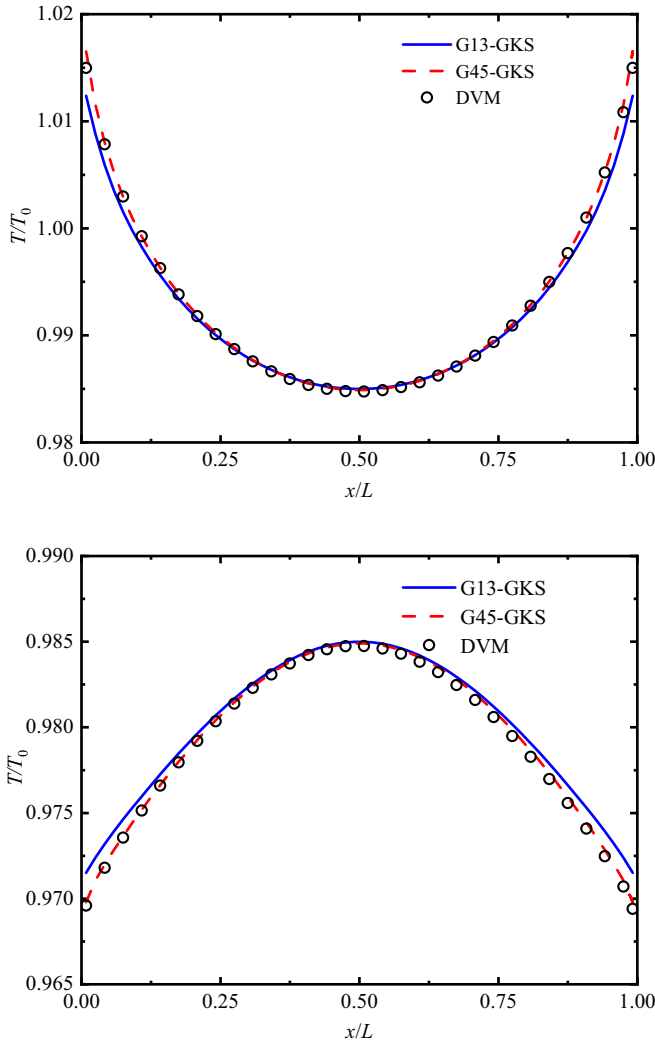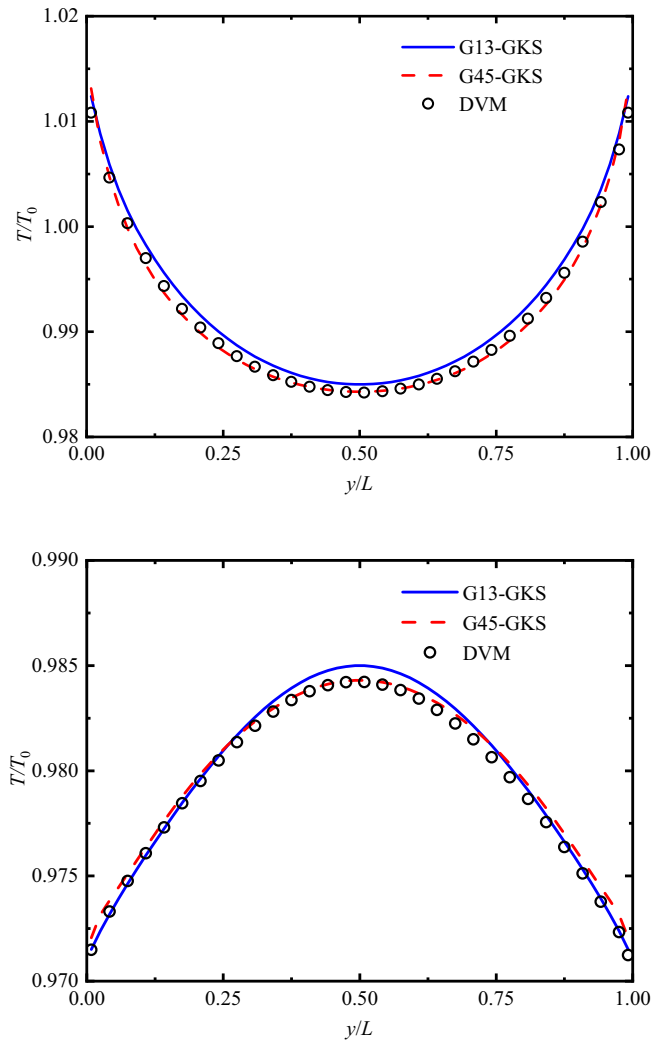

FIG. 10. Temperature along the vertical centerline (top) and horizontal centerline (bottom) of the cavity for Kn = 0.3.

obtained from the incompressible Navier-Stokes solver [61], the CGKS [53], the G13-GKS, and the G45-GKS are shown in Figs. 16–18. From these figures, we can see that the results obtained by the G45-GKS are pretty accurate, and they are the same as the results obtained by the G13-GKS. Therefore, we can conclude that the present solver is quite accurate for flows in the continuum regime, and the high order moments have little effect on the results when the flow is in the continuum regime.

D. Case 4: Thermal transpiration flow

In the last test case, the ability of the present solver to capture the direction of heat flux without temperature gradients is validated. In this test case, the ability of the present solver to capture another important rarefied effect, the thermal creep, is examined. This test case was studied by Masters and Ye [66] using the OSIP-DSMC method, by Xu *et al.* [39] using the UGKS, and by Yang *et al.* [67] using the DVM. The schematic diagram of this test case is shown in Fig. 19, where we consider a sealed two-dimensional microchannel whose length is five times the width. The computational

domain is divided uniformly into 200×40 cells, and the Gauss-Hermite quadrature with 28×28 mesh points is used for the DVM. The left wall of the channel is set as $T_1 = 273$ K, while the right wall of the channel is set as $T_2 = 573$ K. At the top and bottom walls, the temperature varies linearly along the channel. The pressure inside the channel is initialized uniformly as 1 atm, such that the mean free path of gas molecules is 64 nm [39]. In the previous work [39], it was reported that when the flow is in the continuum regime, the Navier-Stokes (NS) equations predict a uniform pressure solution and a pure diffusion temperature solution without velocity field. When the flow turns to a free molecular regime, the pressure is no longer uniform, and the fluid molecules will creep from the low temperature region to the high temperature region, which is called thermal creep flow [5]. And the effect of thermal creep flow has been applied in Knudsen pumps such as micropumps and macroscale vacuum pumps [68].

The pressures along the horizontal centerline for different Knudsen numbers are shown in Fig. 20. Since the flows are in the transition regime in this test case, the pressure is not uniform, and the gradient of the pressure increases as
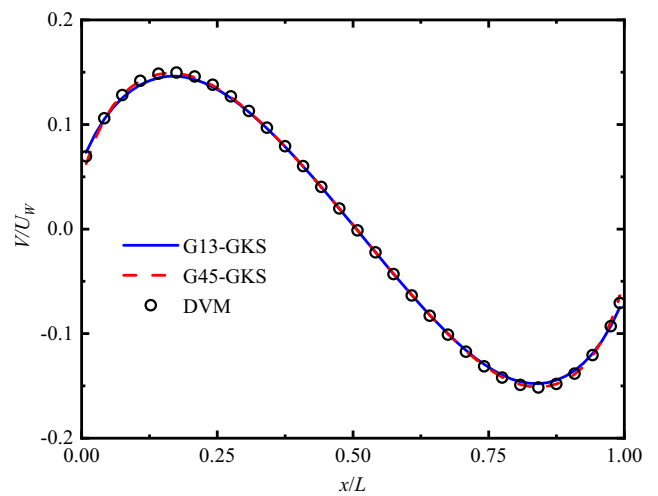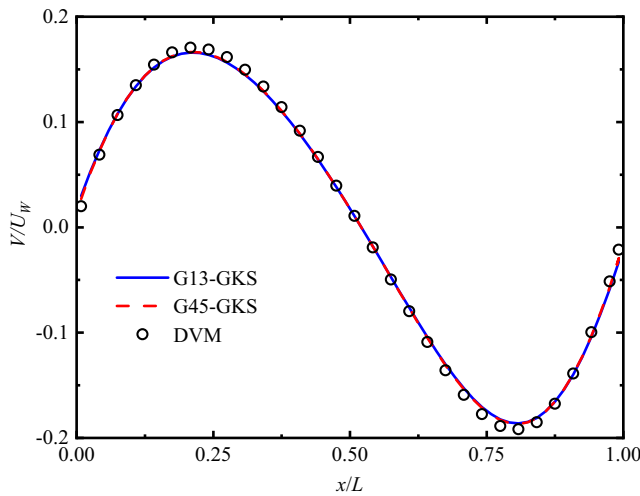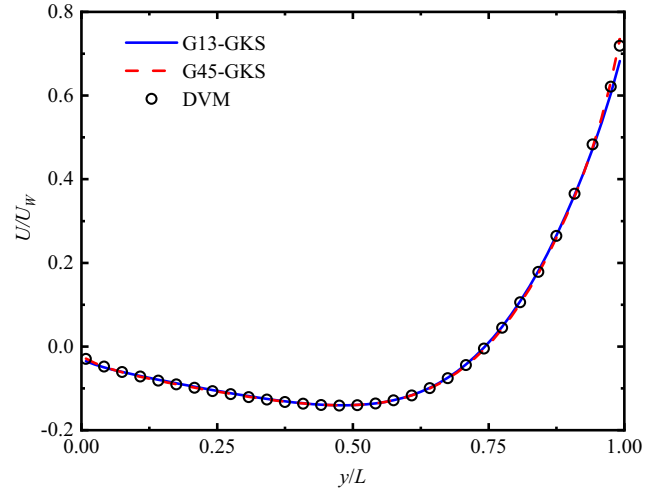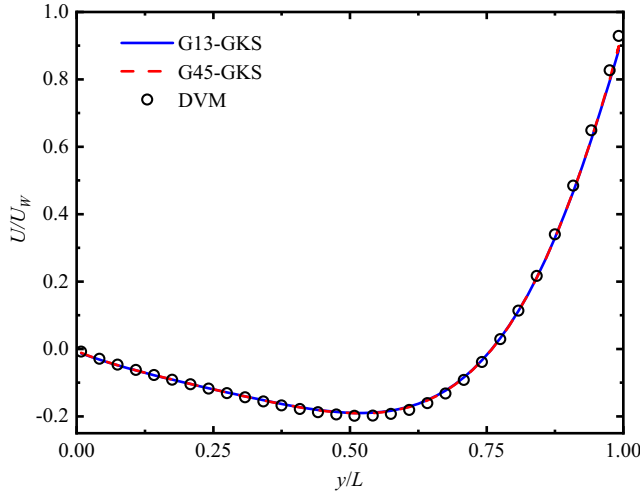
FIG. 11. U velocity along the vertical centerline (top) and V velocity along the horizontal centerline (bottom) of the cavity for Kn = 0.01.

FIG. 12. U velocity along the vertical centerline (top) and V velocity along the horizontal centerline (bottom) of the cavity for Kn = 0.075.

the Knudsen number increases. When Kn is equal to 0.016 (the width of the channel is 4 μm), the gradient of pressure is quite small. We can see that the gradient of pressure predicted by the G13-GKS is larger than that predicted by the DVM [67], while the gradient of pressure predicted by the G45-GKS is close to that predicted by the DVM. For larger Knudsen numbers (Kn = 0.064 and 0.16, the widths of the channel are 1 μm and 400 nm), the profiles of pressure predicted by the G13-GKS deviate from those predicted by the G45-GKS apparently, while the pressures obtained by the G45-GKS can match the DVM data basically. When the Knudsen number reaches 0.64 (the width of the channel is 100 nm), the results obtained by the G13-GKS and G45-GKS cannot match the DVM data well. Nevertheless, the G45-GKS can achieve a much better accuracy compared with the G13-GKS.

Next, the temperature contours and streamlines obtained by the DVM, G13-GKS, and G45-GKS for different Knudsen numbers are shown in Fig. 21 to demonstrate that the

present solver has the ability to capture the thermal creep flow. From Fig. 21 we can see that when Kn = 0.016 and 0.064, the temperature contours and streamlines predicted by the DVM, G13-GKS, and G45-GKS are almost the same. When Kn is increased to 0.16, the streamlines obtained by the DVM and G45-GKS are the same, but the streamlines obtained by the G13-GKS are not smooth. Under these three Knudsen numbers, the flows go from the high temperature region to the low temperature region along the horizontal centerline of the channel. When Kn is increased to 0.64, thermal creep occurs, and flows go from the low temperature region to the high temperature region along the horizontal centerline, and we can see that both the G13-GKS and G45-GKS can capture this phenomenon well. Compared with the G13-GKS, the G45-GKS can predict streamlines closer to those predicted by the DVM. All these results demonstrate that the G45-GKS is much more accurate than the G13-GKS.
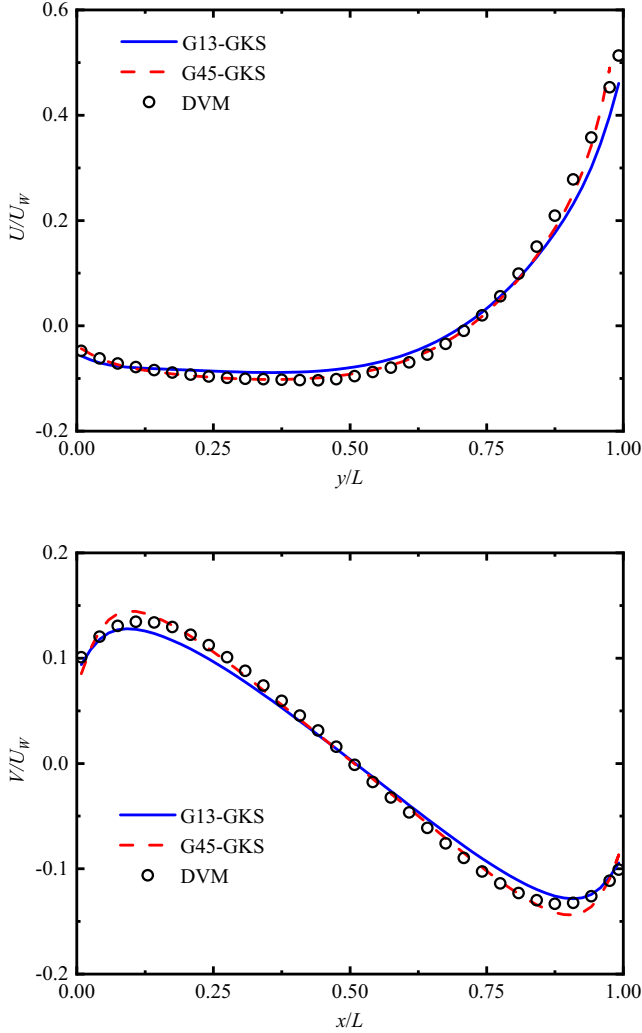
FIG. 13. U velocity along the vertical centerline (top) and V velocity along the horizontal centerline (bottom) of the cavity for Kn = 0.3.

E. Case 5: One-dimensional shock structure

In the last test case, the performance of the G45-GKS for the shock problem is examined. This test case was studied by the DVM by Yang *et al.* [17]. The reference viscosity is given by $\mu_0 = (5\sqrt{\pi}\rho_0 U_0 L_0)\text{Kn}_0/16$, where the reference states ρ_0, U_0, and L_0 are set as 1. The dynamic viscosity is given by Eq. (66) with $w = 0.5$. In this test case, the reference Knudsen number Kn_0 is set as 1, and different Mach numbers (Ma = 1.2 and 1.6) are used to simulate the shock problem. For Ma = 1.2, the computational domain is $x \in [-25, 25]$, while the computational domain is $x \in [-10, 10]$ for Ma = 1.6. In this simulation, these computational domains are discretized uniformly into 100 cells. When Ma = 1.2, the results of density, stress, and heat flux are shown in Fig. 22. For this small Mach number, both the G13-GKS and the G45-GKS can predict accurate results. Furthermore, the Mach number is increased to 1.6, and the results are shown in Fig. 23. Under such Mach number, the results of the G13-GKS deviate from those of the DVM apparently, while the results of the G45-GKS can still match those of the DVM.
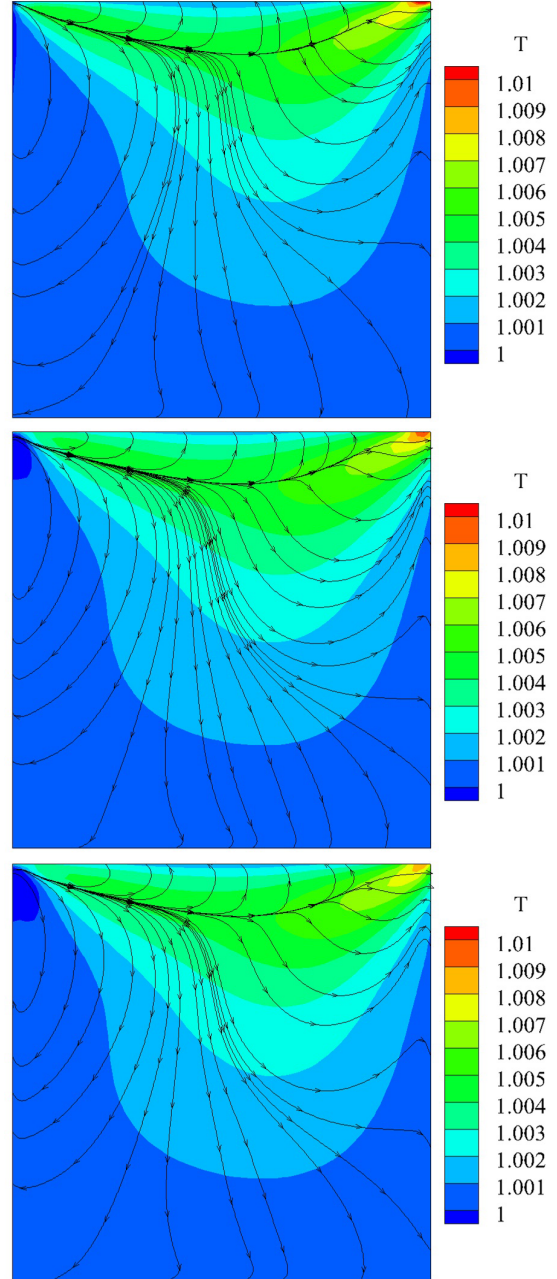

FIG. 14. Temperature contours and corresponding heat fluxes of DVM (top), G13-GKS (middle), and G45-GKS (bottom) for Kn = 0.01.

It can be seen from these results that the accuracy of the G45-GKS is better than that of the G13-GKS for the shock problem.

IV. CONCLUSIONS

In order to improve the accuracy of the G13-GKS, the explicit formulations of the G45 function-based gas kinetic scheme (G45-GKS) are developed in this work. Similar to the G13-GKS, the G45-GKS simulates flows from the continuum regime to the rarefied regime by solving the macroscopic governing equations based on the conservation laws. During
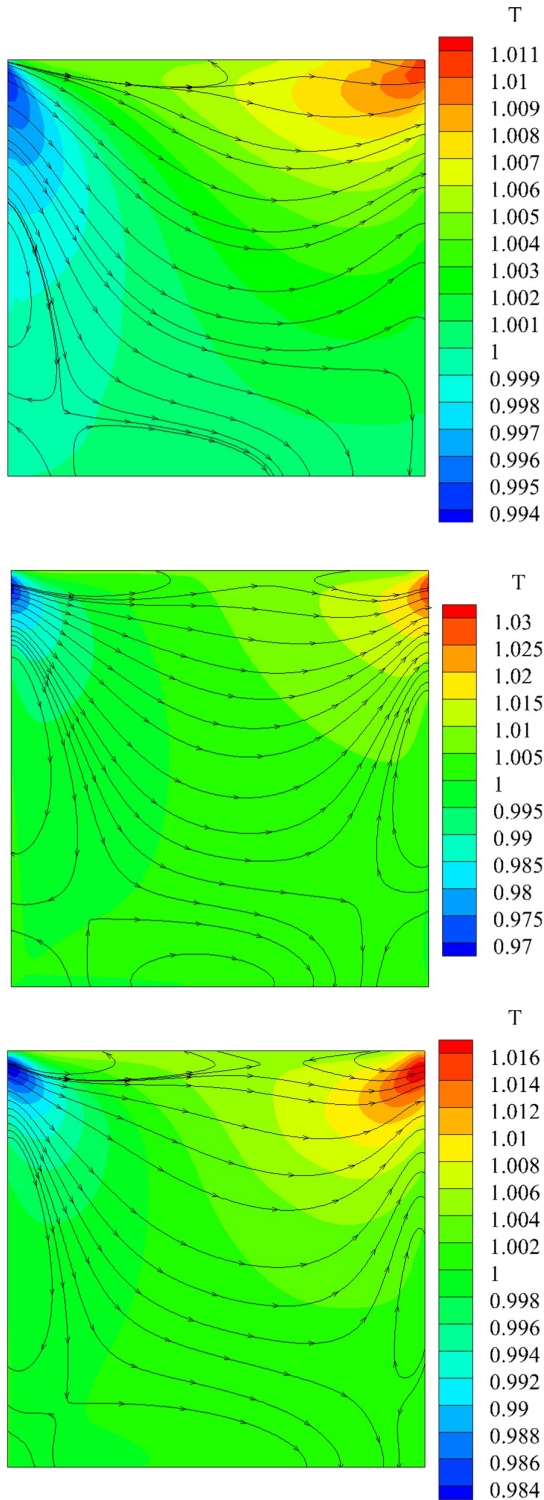
FIG. 15. Temperature contours and corresponding heat fluxes of DVM (top), G13-GKS (middle), and G45-GKS (bottom) for Kn = 0.15.
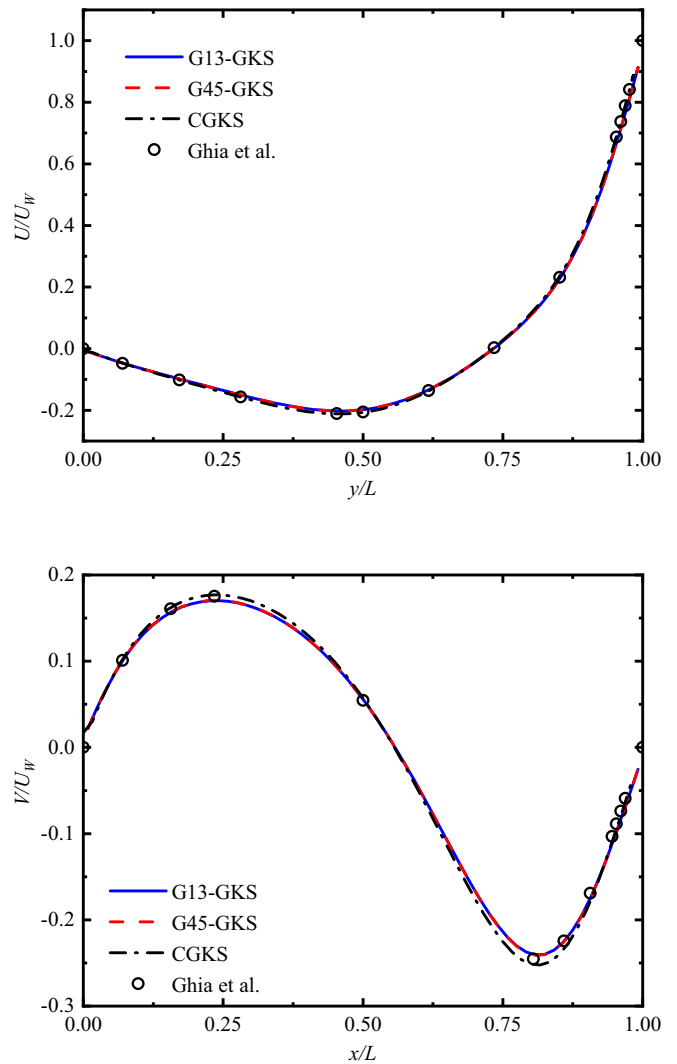

FIG. 16. U velocity along the vertical centerline (top) and V velocity along the horizontal centerline (bottom) of the cavity for Re = 100.

function, namely the Grad's distribution function. To achieve better accuracy than the G13-GKS, the Hermite expansion is truncated partly to the fifth order, which is the G45 distribution function. Thanks to the high order truncation of Hermite expansion, the G45-GKS can achieve much better accuracy than the G13-GKS. After the reconstruction, the evolution of distribution function is avoided, and the numerical fluxes are evaluated by the local solution to the Boltzmann equation. Therefore, the G45-GKS can achieve a much better computational efficiency compared with the DVM.

Several numerical examples are simulated to test the accuracy of the present solver. According to the numerical results obtained, the G45-GKS can predict accurate results for flows in the continuum regime. For flows in the rarefied regime, the accuracy of the G45-GKS is much improved compared with the G13-GKS although more computational time is needed. Thanks to the improvement of accuracy, the G45-GKS can access a wider range of Knudsen numbers than the G13-GKS, which makes the G45-GKS a more attractive method for some practical multiscale flow problems.
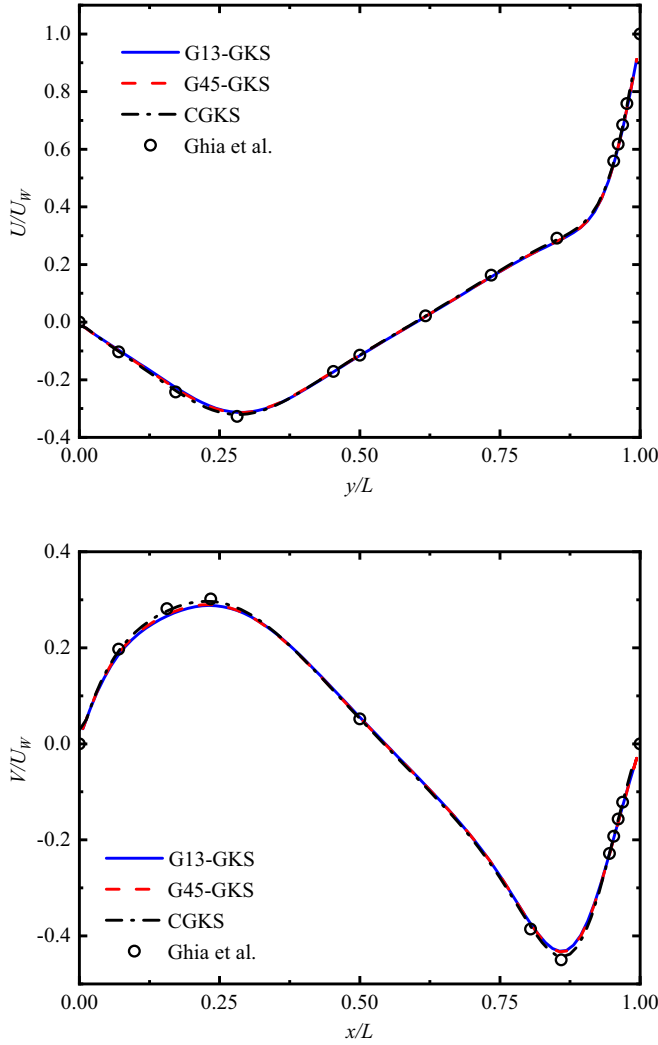
the solution process, the governing equations are discretized by the FVM, and the numerical fluxes are evaluated by a local solution to the Boltzmann equation. To simulate flows in the rarefied regime, the initial distribution function is reconstructed by the truncated Hermite expansion of distribution

FIG. 17. U velocity along the vertical centerline (top) and V velocity along the horizontal centerline (bottom) of the cavity for Re = 400.
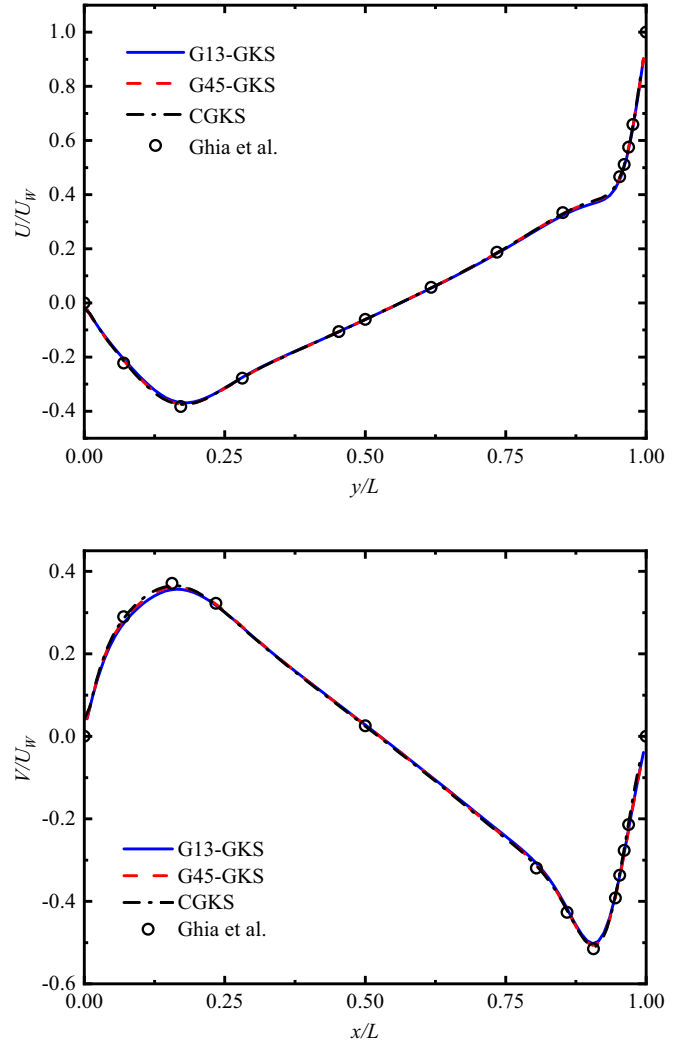

FIG. 18. U velocity along the vertical centerline (top) and V velocity along the horizontal centerline (bottom) of the cavity for Re = 1000.

APPENDIX A: COMPLETE SET OF FORMULATIONS OF THE MOMENT INTEGRALS OF G45 DISTRIBUTION FUNCTION

In this appendix, the complete set of formulations of the moment integrals of the G45 distribution function used in Sec. II C will be given. In Sec. II C, $\langle \xi_x^i C_y^j \zeta^k \rangle_{>0}$ is given in Eq. (40), and $\Phi(\sigma)$ is given in Eq. (39). In this appendix, $\Phi(q)$, $\Phi(m)$, $\Phi(R)$, $\Phi(\Delta)$, $\Phi(\phi)$, $\Phi(\psi)$, and $\Phi(\Omega)$ will be given to complete the full formulation of $\langle \xi_x^i C_y^j \zeta^k \rangle_{>0}$:

$$
\begin{aligned}
\Phi(q) = {} & 0.4\lambda \frac{q_x}{pRT} \langle \xi_x^i C_x^1 C_y^j \zeta^k C^2 \rangle_{>0}^e \\
& + 0.4\lambda \frac{q_y}{pRT} \langle \xi_x^i C_x^0 C_y^{j+1} \zeta^k C^2 \rangle_{>0}^e \\
& - \frac{q_x}{pRT} \langle \xi_x^i C_x^1 C_y^j \zeta^k \rangle_{>0}^e - \frac{q_y}{pRT} \langle \xi_x^i C_x^0 C_y^{j+1} \zeta^k \rangle_{>0}^e,
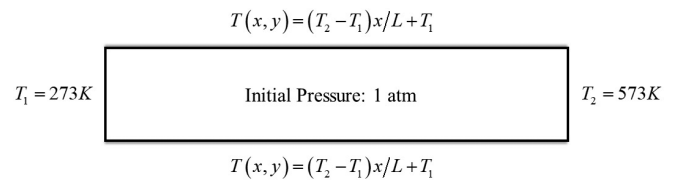\end{aligned}
$$

(A1)

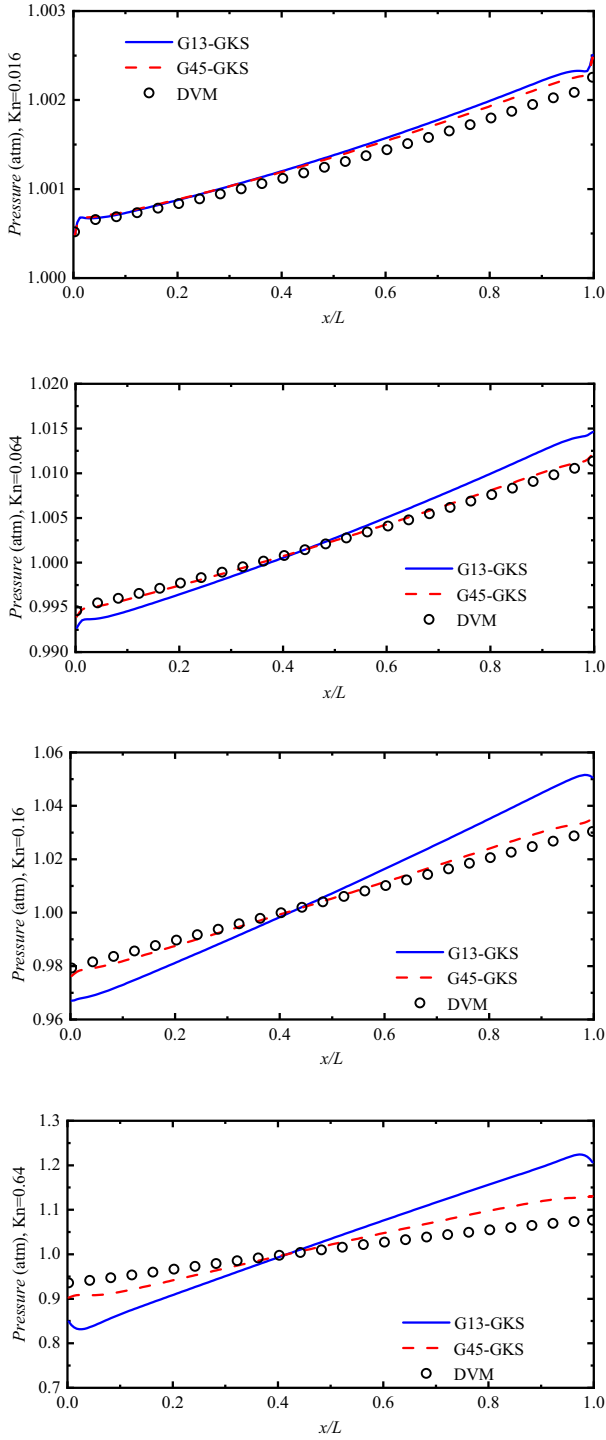

FIG. 19. Schematic diagram of thermal transpiration flow.

FIG. 20. Pressure along the horizontal centerline for Kn $= 0.016$ (top left), Kn $= 0.064$ (top right), Kn $= 0.16$ (bottom left), Kn $= 0.64$ (bottom right).
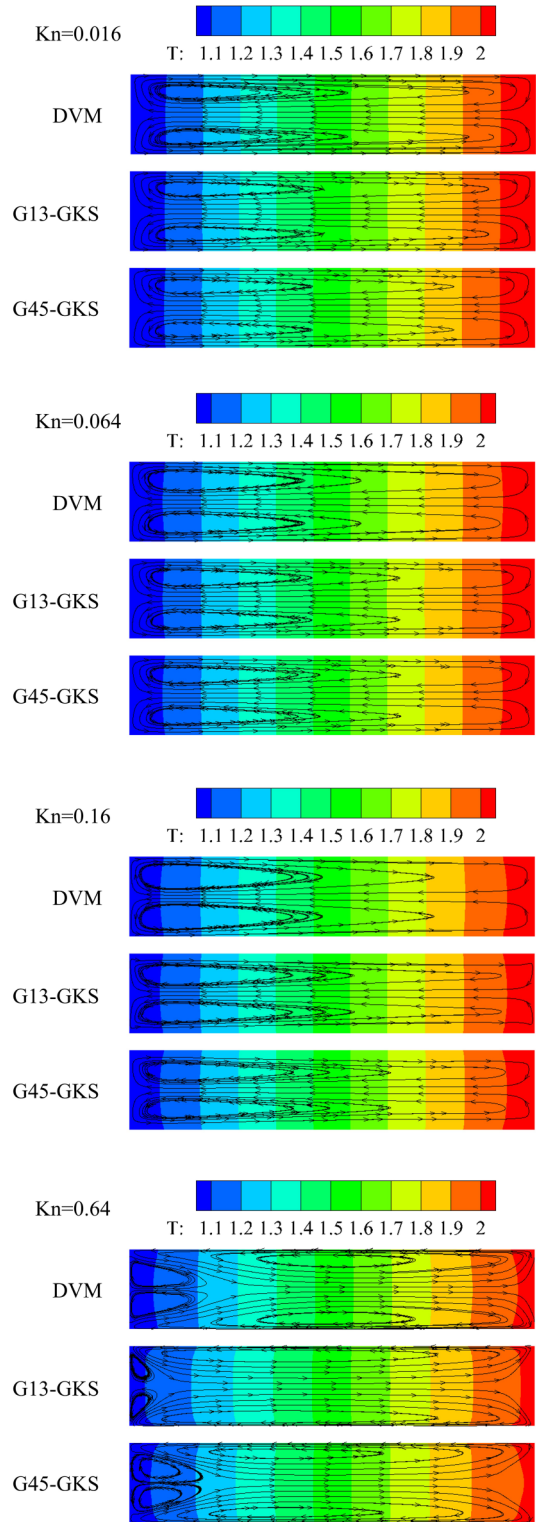

FIG. 21. Temperature contours and streamlines for Kn $= 0.016$, Kn $= 0.064$, Kn $= 0.16$, Kn $= 0.64$.

$$\Phi(m) = \frac{m_{xxx}}{6p(RT)^2}\langle\xi_x^i C_x^3 C_y^j \zeta^k\rangle_{>0}^e + 3\frac{m_{xyy}}{6p(RT)^2}\langle\xi_x^i C_x^1 C_y^{j+2} \zeta^k\rangle_{>0}^e$$

$$- 3\left(\frac{m_{xxx}}{6p(RT)^2} + \frac{m_{xyy}}{6p(RT)^2}\right)\langle\xi_x^i C_x^1 C_y^j \zeta^{k+2}\rangle_{>0}^e$$

$$+ \frac{m_{yyy}}{6p(RT)^2}\langle\xi_x^i C_x^0 C_y^{j+3} \zeta^k\rangle_{>0}^e$$

$$+ 3\frac{m_{xxy}}{6p(RT)^2}\langle\xi_x^i C_x^2 C_y^{j+1} \zeta^k\rangle_{>0}^e$$

$$- 3\left(\frac{m_{xxy}}{6p(RT)^2} + \frac{m_{yyy}}{6p(RT)^2}\right)\langle\xi_x^i C_x^0 C_y^{j+1} \zeta^{k+2}\rangle_{>0}^e, \tag{A2}$$
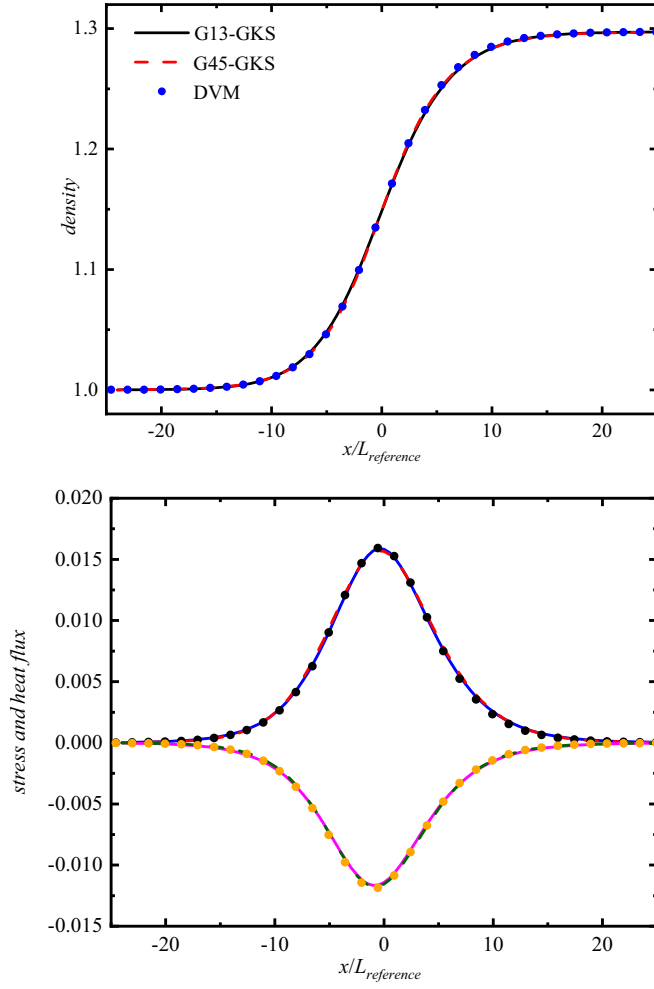
FIG. 22. Density (top), stress, and heat flux (bottom) of one-dimensional (1D) shock structure with Ma $= 1.2$. Red dashed line: stress of G13-GKS; blue line: stress of G45-GKS; black circle: stress of DVM; dark green dashed line: heat flux of G13-GKS; magenta line: heat flux of G45-GKS; orange circle: heat flux of DVM.
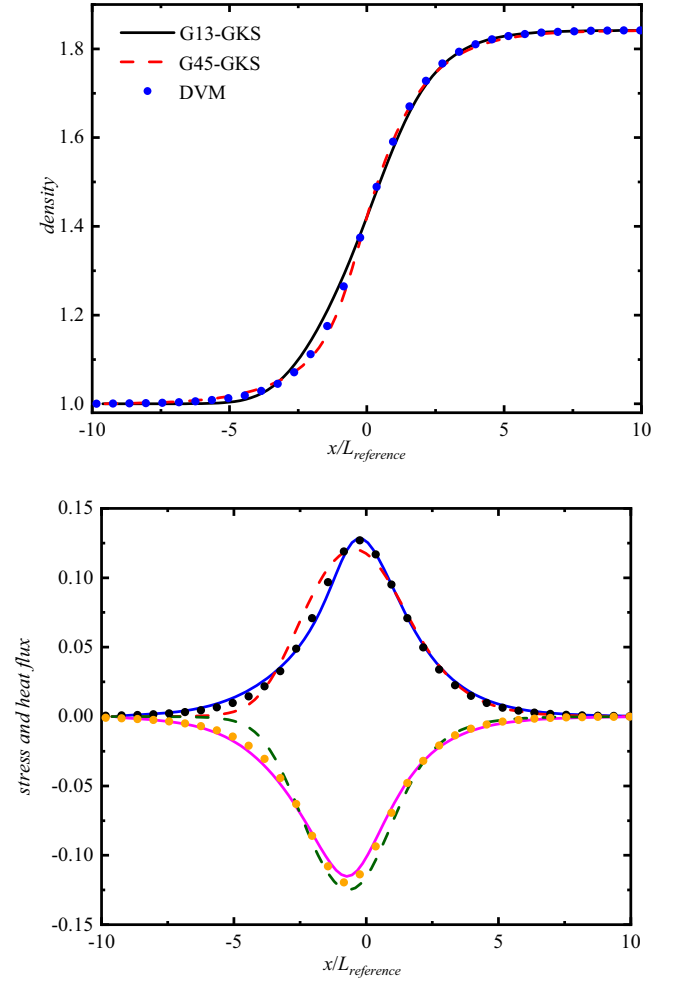

FIG. 23. Density (top), stress and heat flux (bottom) of 1D shock structure with Ma $= 1.6$. red dashed line: stress of G13-GKS; blue line: stress of G45-GKS; black circle: stress of DVM; dark green dashed line: heat flux of G13-GKS; magenta line: heat flux of G45-GKS; orange circle: heat flux of DVM.

$$
\begin{aligned}
\Phi(R) &= \frac{R_{xx}}{4p(RT)^2}\left(\frac{2\lambda}{7}\langle\xi_x^i C_x^2 C_y^j \zeta^k C^2\rangle_{>0}^e - \langle\xi_x^i C_x^2 C_y^j \zeta^k\rangle_{>0}^e\right) \\
&+ 2\frac{R_{xy}}{4p(RT)^2}\left(\frac{2\lambda}{7}\langle\xi_x^i C_x^1 C_y^{j+1} \zeta^k C^2\rangle_{>0}^e - \langle\xi_x^i C_x^1 C_y^{j+1} \zeta^k\rangle_{>0}^e\right) \\
&+ \frac{R_{yy}}{4p(RT)^2}\left(\frac{2\lambda}{7}\langle\xi_x^i C_x^0 C_y^{j+2} \zeta^k C^2\rangle_{>0}^e - \langle\xi_x^i C_x^0 C_y^{j+2} \zeta^k\rangle_{>0}^e\right) \\
&- \left(\frac{R_{xx}}{4p(RT)^2} + \frac{R_{yy}}{4p(RT)^2}\right) \\
&\times \left(\frac{2\lambda}{7}\langle\xi_x^i C_x^0 C_y^j \zeta^{k+2} C^2\rangle_{>0}^e - \langle\xi_x^i C_x^0 C_y^j \zeta^{k+2}\rangle_{>0}^e\right), \quad \text{(A3)}
\end{aligned}
$$

$$
\Phi(\Delta) = \frac{\Delta}{8pRT}\left(\frac{4\lambda^2}{15}\langle\xi_x^i C_x^0 C_y^j \zeta^k C^4\rangle_{>0}^e - \frac{4\lambda}{3}\langle\xi_x^i C_x^2 C_y^j \zeta^k C^2\rangle_{>0}^e + \langle\xi_x^i C_x^0 C_y^j \zeta^k\rangle_{>0}^e\right), \quad \text{(A4)}
$$

$$
\begin{aligned}
\Phi(\phi) &= \frac{\phi_{xxxx}}{24p(RT)^3}\langle\xi_x^i C_x^4 C_y^j \zeta^k\rangle_{>0}^e + \frac{\phi_{yyyy}}{24p(RT)^3}\langle\xi_x^i C_x^0 C_y^{j+4} \zeta^k\rangle_{>0}^e \\
&+ 4\frac{\phi_{xxxy}}{24p(RT)^3}\langle\xi_x^i C_x^3 C_y^{j+1} \zeta^k\rangle_{>0}^e \\
&+ 4\frac{\phi_{xyyy}}{24p(RT)^3}\langle\xi_x^i C_x^1 C_y^{j+3} \zeta^k\rangle_{>0}^e \\
&+ 6\frac{\phi_{xxyy}}{24p(RT)^3}\langle\xi_x^i C_x^2 C_y^{j+2} \zeta^k\rangle_{>0}^e \\
&- 6\left(\frac{\phi_{xxxx}}{24p(RT)^3} + \frac{\phi_{xxyy}}{24p(RT)^3}\right)\langle\xi_x^i C_x^2 C_y^j \zeta^{k+2}\rangle_{>0}^e \\
&- 6\left(\frac{\phi_{xxyy}}{24p(RT)^3} + \frac{\phi_{yyyy}}{24p(RT)^3}\right)\langle\xi_x^i C_x^0 C_y^{j+2} \zeta^{k+2}\rangle_{>0}^e \\
&- 12\left(\frac{\phi_{xxxy}}{24p(RT)^3} + \frac{\phi_{xyyy}}{24p(RT)^3}\right)\langle\xi_x^i C_x^1 C_y^1 \zeta^{k+2}\rangle_{>0}^e \\
&+ \left(\frac{\phi_{xxxx}}{24p(RT)^3} + 2\frac{\phi_{xxyy}}{24p(RT)^3} + \frac{\phi_{yyyy}}{24p(RT)^3}\right) \\
&\times \langle\xi_x^i C_x^0 C_y^j \zeta^{k+4}\rangle_{>0}^e, \quad \text{(A5)}
\end{aligned}
$$

$$\Phi(\psi) = \frac{\psi_{xxx}}{12p(RT)^3}\left(\frac{2\lambda}{9}\langle\xi_x^i C_x^3 C_y^j \zeta^k C^2\rangle_{>0}^e - \langle\xi_x^i C_x^3 C_y^j \zeta^k\rangle_{>0}^e\right)$$

$$+ 3\frac{\psi_{xyy}}{12p(RT)^3}\left(\frac{2\lambda}{9}\langle\xi_x^i C_x^1 C_y^{j+2} \zeta^k C^2\rangle_{>0}^e - \langle\xi_x^i C_x^1 C_y^{j+2} \zeta^k\rangle_{>0}^e\right)$$

$$+ 3\frac{\psi_{xxy}}{12p(RT)^3}\left(\frac{2\lambda}{9}\langle\xi_x^i C_x^2 C_y^{j+1} \zeta^k C^2\rangle_{>0}^e - \langle\xi_x^i C_x^2 C_y^{j+1} \zeta^k\rangle_{>0}^e\right)$$

$$+ \frac{\psi_{yyy}}{12p(RT)^3}\left(\frac{2\lambda}{9}\langle\xi_x^i C_x^0 C_y^{j+3} \zeta^k C^2\rangle_{>0}^e - \langle\xi_x^i C_x^0 C_y^{j+3} \zeta^k\rangle_{>0}^e\right)$$

$$- 3\left(\frac{\psi_{xxx}}{12p(RT)^3} + \frac{\psi_{xyy}}{12p(RT)^3}\right)\left(\frac{2\lambda}{9}\langle\xi_x^i C_x^1 C_y^j \zeta^{k+2} C^2\rangle_{>0}^e - \langle\xi_x^i C_x^1 C_y^j \zeta^{k+2}\rangle_{>0}^e\right)$$

$$- 3\left(\frac{\psi_{xxy}}{12p(RT)^3} + \frac{\psi_{yyy}}{12p(RT)^3}\right)\left(\frac{2\lambda}{9}\langle\xi_x^i C_x^0 C_y^{j+1} \zeta^{k+2} C^2\rangle_{>0}^e - \langle\xi_x^i C_x^0 C_y^{j+1} \zeta^{k+2}\rangle_{>0}^e\right), \tag{A6}$$

$$\Phi(\Omega) = \frac{\Omega_x}{40p(RT)^2}\left(\frac{4\lambda^2}{7}\langle\xi_x^i C_x^1 C_y^j \zeta^k C^4\rangle_{>0}^e - 4\lambda\langle\xi_x^i C_x^1 C_y^j \zeta^k C^2\rangle_{>0}^e + 5\langle\xi_x^i C_x^1 C_y^j \zeta^k\rangle_{>0}^e\right)$$

$$+ \frac{\Omega_y}{40p(RT)^2}\left(\frac{4\lambda^2}{7}\langle\xi_x^i C_x^0 C_y^{j+1} \zeta^k C^4\rangle_{>0}^e - 4\lambda\langle\xi_x^i C_x^0 C_y^{j+1} \zeta^k C^2\rangle_{>0}^e + 5\langle\xi_x^i C_x^0 C_y^{j+1} \zeta^k\rangle_{>0}^e\right). \tag{A7}$$

APPENDIX B: BASIC FORMULATIONS OF HIGH ORDER MOMENTS

In Sec. II D, the formulations of stresses and heat fluxes are given with the help of Λ_{ijk}. Next, other high order moments, such as m_{ijk}, R_{ij}, Δ, ϕ_{ijkl}, ψ_{ijk}, and Ω_i introduced in Eqs. (15)–(28) should also be calculated. In this appendix, the explicit formulations of other high order moments are given with the help of Λ_{ijk} defined by Eq. (54):

$$m_{xxx} = \Lambda_{300} - \tfrac{3}{5}(\Lambda_{300} + \Lambda_{120} + \Lambda_{102}),$$
$$m_{xyy} = \Lambda_{120} - \tfrac{1}{5}(\Lambda_{300} + \Lambda_{120} + \Lambda_{102}),$$
$$m_{yyy} = \Lambda_{030} - \tfrac{3}{5}(\Lambda_{210} + \Lambda_{030} + \Lambda_{012}),$$
$$m_{xxy} = \Lambda_{210} - \tfrac{1}{5}(\Lambda_{210} + \Lambda_{030} + \Lambda_{012}), \tag{B1}$$

$$R_{xx} = \tfrac{1}{3}(2\Lambda_{400} + \Lambda_{220} - \Lambda_{040} + \Lambda_{202} - 2\Lambda_{022} - \Lambda_{004}) - 7\sigma_{xx},$$
$$R_{xy} = \tfrac{1}{3}(\Lambda_{310} + \Lambda_{130} + \Lambda_{112}) - 7\sigma_{xy},$$
$$R_{yy} = \tfrac{1}{3}(-\Lambda_{400} + \Lambda_{220} + 2\Lambda_{040} - 2\Lambda_{202} + \Lambda_{022} - \Lambda_{004}) - 7\sigma_{yy}, \tag{B2}$$

$$\Delta = \Lambda_{400} + 2\Lambda_{220} + \Lambda_{040} + 2\Lambda_{202} + \Lambda_{022} + \Lambda_{040} - 15\frac{\delta t}{\tau + \delta t}\rho(RT)^2, \tag{B3}$$

$$\phi_{xxxx} = \tfrac{1}{35}(8\Lambda_{400} - 24\Lambda_{220} - 24\Lambda_{202} + 3\Lambda_{040} + 6\Lambda_{022} + 3\Lambda_{004}),$$
$$\phi_{xxyy} = \tfrac{1}{35}(-4\Lambda_{400} + 27\Lambda_{220} - 3\Lambda_{202} - 4\Lambda_{040} - 3\Lambda_{022} + \Lambda_{004}),$$
$$\phi_{yyyy} = \tfrac{1}{35}(3\Lambda_{400} - 24\Lambda_{220} + 6\Lambda_{202} + 8\Lambda_{040} - 24\Lambda_{022} + 3\Lambda_{004}),$$
$$\phi_{xxxy} = \tfrac{1}{7}(4\Lambda_{310} - 3\Lambda_{130} - 3\Lambda_{112}),$$
$$\phi_{xyyy} = \tfrac{1}{7}(-3\Lambda_{310} + 4\Lambda_{130} - 3\Lambda_{112}), \tag{B4}$$

$$\psi_{xxx} = \tfrac{1}{5}(2\Lambda_{500} - \Lambda_{320} - 3\Lambda_{140} - \Lambda_{302} - 6\Lambda_{122} - 3\Lambda_{104}) - 9RT m_{xxx},$$
$$\psi_{xyy} = \tfrac{1}{5}(-\Lambda_{500} + 3\Lambda_{320} + 4\Lambda_{140} - 2\Lambda_{302} + 3\Lambda_{122} - \Lambda_{104}) - 9RT m_{xyy},$$
$$\psi_{xxy} = \tfrac{1}{5}(4\Lambda_{140} + 3\Lambda_{230} - \Lambda_{050} + 3\Lambda_{212} - 2\Lambda_{032} - \Lambda_{014}) - 9RT m_{xxy},$$
$$\psi_{yyy} = \tfrac{1}{5}(-3\Lambda_{140} - \Lambda_{230} + 2\Lambda_{050} - 6\Lambda_{212} - \Lambda_{032} - 3\Lambda_{014}) - 9RT m_{yyy}, \tag{B5}$$

$$\Omega_x = \Lambda_{500} + 2\Lambda_{320} + \Lambda_{140} + 2\Lambda_{302} + 2\Lambda_{122} + \Lambda_{104} - 28RT q_x,$$

$$\Omega_y = \Lambda_{410} + 2\Lambda_{230} + \Lambda_{050} + 2\Lambda_{212} + 2\Lambda_{032} + \Lambda_{014} - 28RT q_y. \tag{B6}$$

APPENDIX C: BASIC FORMULATIONS OF NUMERICAL FLUXES AND HIGH ORDER MOMENTS AT THE HORIZONTAL CELL INTERFACE (IN THE y DIRECTION)

In the main text of this paper, the numerical fluxes and high order moments at the vertical cell interface (in the x direction) are given. In this appendix, the explicit formulations of numerical fluxes and high order moments at the horizontal cell interface (in the y direction) will be given. Similar to numerical fluxes in the x direction, the numerical fluxes in the y direction can also be derived from the moment integrals of the G45 distribution functions $\langle \xi_x^i \xi_y^j \zeta^k \rangle_{>0}$ and $\langle \xi_x^i \xi_y^j \zeta^k \rangle_{<0}$ with their derivatives. In this appendix, $\langle \cdots \rangle_{>0}$ or $\langle \cdots \rangle_{<0}$ mean that the integral domain of ξ_y is $(0, +\infty)$ or $(-\infty, 0)$, while the integral domain of ξ_x and ζ is $(-\infty, +\infty)$. To calculate $\langle \xi_x^i \xi_y^j \zeta^k \rangle_{>0}$ and $\langle \xi_x^i \xi_y^j \zeta^k \rangle_{<0}$, the moment integrals of $\langle C_x^i \xi_y^j \zeta^k \rangle_{>0}$ and $\langle C_x^i \xi_y^j \zeta^k \rangle_{<0}$ are calculated first. To calculate $\langle C_x^i \xi_y^j \zeta^k \rangle_{>0}$ and $\langle C_x^i \xi_y^j \zeta^k \rangle_{<0}$, the moment integrals are needed. The moment integrals of the Maxwellian distribution function should be given first. In the main text, $\langle C_x^n \rangle^e$, $\langle C_y^n \rangle^e$, and $\langle \zeta^n \rangle^e$ have been given by Eq. (34), and the moment integrals of $\langle \xi_y^n \rangle_{>0}^e$ and $\langle \xi_y^n \rangle_{<0}^e$ are given as

$$\langle \xi_y^0 \rangle_{>0}^e = \frac{1}{2}[1 + \mathrm{erf}(\sqrt{\lambda^l}V^l)],$$

$$\langle \xi_y^1 \rangle_{>0}^e = V^l \langle \xi_y^0 \rangle_{>0}^e + \frac{1}{2}\frac{e^{-\lambda^l(V^l)^2}}{\sqrt{\lambda^l \pi}},$$

$$\langle \xi_y^{k+2} \rangle_{>0}^e = U^l \langle \xi_y^{k+1} \rangle_{>0}^e + \frac{k+1}{2\lambda^l}\langle \xi_y^k \rangle_{>0}^e, k = 0, 1, 2, \ldots \tag{C1}$$

and

$$\langle \xi_y^0 \rangle_{<0}^e = \frac{1}{2}\mathrm{erfc}(\sqrt{\lambda^r}V^r),$$

$$\langle \xi_y^1 \rangle_{<0}^e = V^r \langle \xi_y^0 \rangle_{<0}^e - \frac{1}{2}\frac{e^{-\lambda^r(V^r)^2}}{\sqrt{\lambda^r \pi}},$$

$$\langle \xi_y^{k+2} \rangle_{<0}^e = V^r \langle \xi_y^{k+1} \rangle_{<0}^e + \frac{k+1}{2\lambda^r}\langle \xi_y^k \rangle_{<0}^e, k = 0, 1, 2, \ldots, \tag{C2}$$

where l and r mean the bottom side and the upper side of cell interface. Take the moment integrals at the bottom side of cell interface as an example. At first, we need to calculate the moments:

$$\langle \xi_y^j C_x^i C_y^n \zeta^k \rangle_{>0}^e = \langle C_x^i \rangle^e \langle \xi_y^j C_y^n \rangle_{>0}^e \langle \zeta^k \rangle^e, \tag{C3}$$

where $\langle \xi_y^k C_y^n \rangle_{>0}^e$ is calculated by binomial theorem as

$$\langle \xi_y^k C_y^n \rangle_{>0}^e = (-1)^{n-m}\sum_{m=0}^{n}\frac{n!}{m!(n-m)!}\langle \xi_y^{m+k} \rangle_{>0}^e (V^l)^{n-m}. \tag{C4}$$

Next, with the help of $\langle \xi_y^j C_x^i C_y^n \zeta^k \rangle_{>0}^e$, we can calculate $\langle C_x^i \xi_y^j \zeta^k \rangle_{>0}$, which is given as

$$\langle C_x^i \xi_y^j \zeta^k \rangle_{>0} = \langle \xi_y^j C_x^i C_y^0 \zeta^k \rangle_{>0}^e + \Phi(\sigma) + \Phi(q) + \Phi(m) + \Phi(R) + \Phi(\Delta) + \Phi(\phi) + \Phi(\psi) + \Phi(\Omega), \tag{C5}$$

where

$$\Phi(\sigma) = \frac{\sigma_{xx}}{2pRT}\langle \xi_y^j C_x^{i+2} C_y^0 \zeta^k \rangle_{>0}^e + 2\frac{\sigma_{xy}}{2pRT}\langle \xi_y^j C_x^{i+1} C_y^1 \zeta^k \rangle_{>0}^e + \frac{\sigma_{yy}}{2pRT}\langle \xi_y^j C_x^i C_y^2 \zeta^k \rangle_{>0}^e - \left(\frac{\sigma_{xx}}{2pRT} + \frac{\sigma_{yy}}{2pRT}\right)\langle \xi_y^j C_x^i C_y^0 \zeta^{k+2} \rangle_{>0}^e, \tag{C6}$$

$$\Phi(q) = 0.4\lambda\frac{q_x}{pRT}\langle \xi_y^j C_x^{i+1} C_y^0 \zeta^k C^2 \rangle_{>0}^e + 0.4\lambda\frac{q_y}{pRT}\langle \xi_y^j C_x^i C_y^1 \zeta^k C^2 \rangle_{>0}^e - \frac{q_x}{pRT}\langle \xi_y^j C_x^{i+1} C_y^0 \zeta^k \rangle_{>0}^e - \frac{q_y}{pRT}\langle \xi_y^j C_x^i C_y^1 \zeta^k \rangle_{>0}^e, \tag{C7}$$

$$\Phi(m) = \frac{m_{xxx}}{6p(RT)^2}\langle \xi_y^j C_x^{i+3} C_y^0 \zeta^k \rangle_{>0}^e + 3\frac{m_{xyy}}{6p(RT)^2}\langle \xi_y^j C_x^{i+1} C_y^2 \zeta^k \rangle_{>0}^e - 3\left(\frac{m_{xxx}}{6p(RT)^2} + \frac{m_{xyy}}{6p(RT)^2}\right)\langle \xi_y^j C_x^{i+1} C_y^0 \zeta^{k+2} \rangle_{>0}^e$$

$$+ \frac{m_{yyy}}{6p(RT)^2}\langle \xi_y^j C_x^i C_y^3 \zeta^k \rangle_{>0}^e + 3\frac{m_{xxy}}{6p(RT)^2}\langle \xi_y^j C_x^{i+2} C_y^1 \zeta^k \rangle_{>0}^e - 3\left(\frac{m_{xxy}}{6p(RT)^2} + \frac{m_{yyy}}{6p(RT)^2}\right)\langle \xi_y^j C_x^i C_y^1 \zeta^{k+2} \rangle_{>0}^e, \tag{C8}$$

$$\Phi(R) = \frac{R_{xx}}{4p(RT)^2}\left(\frac{2\lambda}{7}\langle \xi_y^j C_x^{i+2} C_y^0 \zeta^k C^2 \rangle_{>0}^e - \langle \xi_y^j C_x^{i+2} C_y^0 \zeta^k \rangle_{>0}^e\right) + 2\frac{R_{xy}}{4p(RT)^2}\left(\frac{2\lambda}{7}\langle \xi_y^j C_x^{i+1} C_y^1 \zeta^k C^2 \rangle_{>0}^e - \langle \xi_y^j C_x^{i+1} C_y^1 \zeta^k \rangle_{>0}^e\right)$$

$$+ \frac{R_{yy}}{4p(RT)^2}\left(\frac{2\lambda}{7}\langle \xi_y^j C_x^i C_y^2 \zeta^k C^2 \rangle_{>0}^e - \langle \xi_y^j C_x^i C_y^2 \zeta^k \rangle_{>0}^e\right)$$

$$- \left(\frac{R_{xx}}{4p(RT)^2} + \frac{R_{yy}}{4p(RT)^2}\right)\left(\frac{2\lambda}{7}\langle \xi_y^j C_x^i C_y^0 \zeta^{k+2} C^2 \rangle_{>0}^e - \langle \xi_y^j C_x^i C_y^0 \zeta^{k+2} \rangle_{>0}^e\right), \tag{C9}$$

$$\Phi(\Delta) = \frac{\Delta}{8pRT}\left(\frac{4\lambda^2}{15}\langle \xi_y^j C_x^i C_y^0 \zeta^k C^4 \rangle_{>0}^e - \frac{4\lambda}{3}\langle \xi_y^j C_x^{i+2} C_y^0 \zeta^k C^2 \rangle_{>0}^e + \langle \xi_y^j C_x^i C_y^0 \zeta^k \rangle_{>0}^e\right), \tag{C10}$$

$$\Phi(\phi) = \frac{\phi_{xxxx}}{24p(RT)^3}\langle\xi_y^j C_x^{i+4} C_y^0 \zeta^k\rangle_{>0}^e + \frac{\phi_{yyyy}}{24p(RT)^3}\langle\xi_y^j C_x^i C_y^4 \zeta^k\rangle_{>0}^e + 4\frac{\phi_{xxxy}}{24p(RT)^3}\langle\xi_y^j C_x^{i+3} C_y^1 \zeta^k\rangle_{>0}^e$$

$$+ 4\frac{\phi_{xyyy}}{24p(RT)^3}\langle\xi_y^j C_x^{i+1} C_y^3 \zeta^k\rangle_{>0}^e + 6\frac{\phi_{xxyy}}{24p(RT)^3}\langle\xi_y^j C_x^{i+2} C_y^2 \zeta^k\rangle_{>0}^e$$

$$- 6\left(\frac{\phi_{xxxx}}{24p(RT)^3} + \frac{\phi_{xxyy}}{24p(RT)^3}\right)\langle\xi_y^j C_x^{i+2} C_y^0 \zeta^{k+2}\rangle_{>0}^e - 6\left(\frac{\phi_{xxyy}}{24p(RT)^3} + \frac{\phi_{yyyy}}{24p(RT)^3}\right)\langle\xi_y^j C_x^i C_y^2 \zeta^{k+2}\rangle_{>0}^e$$

$$- 12\left(\frac{\phi_{xxxy}}{24p(RT)^3} + \frac{\phi_{xyyy}}{24p(RT)^3}\right)\langle\xi_y^j C_x^{i+1} C_y^1 \zeta^{k+2}\rangle_{>0}^e$$

$$+ \left(\frac{\phi_{xxxx}}{24p(RT)^3} + 2\frac{\phi_{xxyy}}{24p(RT)^3} + \frac{\phi_{yyyy}}{24p(RT)^3}\right)\langle\xi_y^j C_x^i C_y^0 \zeta^{k+4}\rangle_{>0}^e, \tag{C11}$$

$$\Phi(\psi) = \frac{\psi_{xxx}}{12p(RT)^3}\left(\frac{2\lambda}{9}\langle\xi_y^j C_x^{i+3} C_y^0 \zeta^k C^2\rangle_{>0}^e - \langle\xi_y^j C_x^{i+3} C_y^0 \zeta^k\rangle_{>0}^e\right)$$

$$+ 3\frac{\psi_{xyy}}{12p(RT)^3}\left(\frac{2\lambda}{9}\langle\xi_y^j C_x^{i+1} C_y^2 \zeta^k C^2\rangle_{>0}^e - \langle\xi_y^j C_x^{i+1} C_y^2 \zeta^k\rangle_{>0}^e\right)$$

$$+ 3\frac{\psi_{xxy}}{12p(RT)^3}\left(\frac{2\lambda}{9}\langle\xi_y^j C_x^{i+2} C_y^1 \zeta^k C^2\rangle_{>0}^e - \langle\xi_y^j C_x^{i+2} C_y^1 \zeta^k\rangle_{>0}^e\right)$$

$$+ \frac{\psi_{yyy}}{12p(RT)^3}\left(\frac{2\lambda}{9}\langle\xi_y^j C_x^i C_y^3 \zeta^k C^2\rangle_{>0}^e - \langle\xi_y^j C_x^i C_y^3 \zeta^k\rangle_{>0}^e\right)$$

$$[4pt] \quad - 3\left(\frac{\psi_{xxx}}{12p(RT)^3} + \frac{\psi_{xyy}}{12p(RT)^3}\right)\left(\frac{2\lambda}{9}\langle\xi_y^j C_x^{i+1} C_y^0 \zeta^{k+2} C^2\rangle_{>0}^e - \langle\xi_y^j C_x^{i+1} C_y^0 \zeta^{k+2}\rangle_{>0}^e\right)$$

$$- 3\left(\frac{\psi_{xxy}}{12p(RT)^3} + \frac{\psi_{yyy}}{12p(RT)^3}\right)\left(\frac{2\lambda}{9}\langle\xi_y^j C_x^i C_y^1 \zeta^{k+2} C^2\rangle_{>0}^e - \langle\xi_y^j C_x^i C_y^1 \zeta^{k+2}\rangle_{>0}^e\right), \tag{C12}$$

$$\Phi(\Omega) = \frac{\Omega_x}{40p(RT)^2}\left(\frac{4\lambda^2}{7}\langle\xi_y^j C_x^{i+1} C_y^0 \zeta^k C^4\rangle_{>0}^e - 4\lambda\langle\xi_y^j C_x^{i+1} C_y^0 \zeta^k C^2\rangle_{>0}^e + 5\langle\xi_y^j C_x^{i+1} C_y^0 \zeta^k\rangle_{>0}^e\right)$$

$$+ \frac{\Omega_y}{40p(RT)^2}\left(\frac{4\lambda^2}{7}\langle\xi_y^j C_x^i C_y^1 \zeta^k C^4\rangle_{>0}^e - 4\lambda\langle\xi_y^j C_x^i C_y^1 \zeta^k C^2\rangle_{>0}^e + 5\langle\xi_y^j C_x^i C_y^1 \zeta^k\rangle_{>0}^e\right). \tag{C13}$$

With the help of Eq. (C6) and the binomial theorem, the $\langle\xi_x^i \xi_y^j \zeta^k\rangle_{>0}$ can be calculated as

$$\langle\xi_x^i \xi_y^j \zeta^k\rangle_{>0} = \sum_{m=0}^{i} \frac{i!}{m!(i-m)!}\langle C_x^m \xi_y^j \zeta^k\rangle_{>0}(U^l)^{i-m}. \tag{C14}$$

Similar to the above strategy, $\langle\xi_x^i \xi_y^j \zeta^k\rangle_{<0}$ can be calculated with the integrals conducted at the upper side of cell interface. With the help of $\langle\xi_x^i \xi_y^j \zeta^k\rangle_{>0}$ and $\langle\xi_x^i \xi_y^j \zeta^k\rangle_{<0}$, the parameter M_{ijk} can be defined by Eq. (43). And the conservative variables at the cell interface can be calculated by Eqs. (44)–(47). Therefore, $\boldsymbol{F}^{y(0)}$ can be calculated from these conservative variables:

$$\boldsymbol{F}^{y(0)} = \begin{pmatrix} \rho V \\ \rho U V \\ \rho V^2 + P \\ (\rho E + p)V \end{pmatrix}, \tag{C15}$$

and the numerical flux $\boldsymbol{F}^{y(1)}$ can be given as

$$F_\rho^{y(1)} = M_{010}, \tag{C16}$$

$$F_{\rho U}^{y(1)} = M_{110}, \tag{C17}$$

$$F_{\rho V}^{x(1)} = M_{020}, \tag{C18}$$

$$F_{\rho E}^{y(1)} = \tfrac{1}{2}(M_{210} + M_{030} + M_{012}). \tag{C19}$$

After calculating the numerical fluxes at the cell interface, the high order moments at the cell interface should be calculated. Starting from M_{ijk}, the parameters Λ_{ijk} can be calculated by Eq. (55). Then the stresses and heat fluxes can be calculated by Eqs. (56) and (57), respectively, and the other high order moments can be calculated by the equations given in Appendix B.

[1] B. D. Todd and D. J. Evans, Temperature profile for poiseuille flow, Phys. Rev. E **55**, 2800 (1997).

[2] F. J. Uribe and A. L. Garcia, Burnett description for plane poiseuille flow, Phys. Rev. E **60**, 4063 (1999).

[3] K. Aoki, S. Takata, and T. Nakanishi, Poiseuille-type flow of a rarefied gas between two parallel plates driven by a uniform external force, Phys. Rev. E **65**, 026315 (2002).

[4] T. Takaishi and Y. Sensui, Thermal transpiration effect of hydrogen, rare gases and methane, Trans. Faraday Soc. **59**, 2503 (1963).

[5] B. K. Annis, Thermal creep in gases, J. Chem. Phys. **57**, 2898 (1972).

[6] H. Yamaguchi, P. Perrier, M. T. Ho, J. G. Méolans, T. Niimi, and I. Graur, Mass flow rate measurement of thermal creep flow from transitional to slip flow regime, J. Fluid Mech. **795**, 690 (2016).

[7] N. Dongari, A. Sharma, and F. Durst, Pressure-driven diffusive gas flows in micro-channels: From the Knudsen to the continuum regimes, Microfluid. Nanofluid. **6**, 679 (2009).

[8] W. Liu, G. Tang, W. Su, L. Wu, and Y. Zhang, Rarefaction throttling effect: Influence of the bend in micro-channel gaseous flow, Phys. Fluids **30**, 082002 (2018).

[9] M. Urbakh, J. Klafter, D. Gourdon, and J. Israelachvili, The nonlinear nature of friction, Nature (London) **430**, 525 (2004).

[10] X. Nie, S. Chen, and M. O. Robbins, Hybrid continuum-atomistic simulation of singular corner flow, Phys. Fluids **16**, 3579 (2004).

[11] X. Nie, M. O. Robbins, and S. Chen, Resolving Singular Forces in Cavity Flow: Multiscale Modeling from Atomic to Millimeter Scales, Phys. Rev. Lett. **96**, 134501 (2006).

[12] G. A. Bird, *Molecular Gas Dynamics and the Direct Simulation of Gas Flows* (Clarendon Press, Oxford, 1994).

[13] C. D. Robinson and J. K. Harvey, Adaptive domain decomposition for unstructured meshes applied to the direct simulation monte carlo method, in *Parallel Computational Fluid Dynamics 1996*, edited by P. Schiano, A. Ecer, J. Periaux, and N. Satofuka (North-Holland, Amsterdam, 1997), pp. 469–476.

[14] A. Mohammadzadeh, E. Roohi, and H. Niazmand, A Parallel DSMC investigation of monatomic/diatomic gas flows in a micro/nano cavity, Numer. Heat Transfer, Part A: Appl. **63**, 305 (2013).

[15] C. K. Chu, Kinetic-theoretic description of shock wave formation. II, Phys. Fluids **8**, 1450 (1965).

[16] V. V. Aristov, *Direct Methods for Solving the Boltzmann Equation and Study of Nonequilibrium Flows* (Springer, Dordrecht, 2012).

[17] L. M. Yang, C. Shu, J. Wu, and Y. Wang, Numerical simulation of flows from free molecular regime to continuum regime by a DVM with streaming and collision processes, J. Comput. Phys. **306**, 291 (2016).

[18] H. Grad, The profile of a steady plane shock wave, Commun. Pure Appl. Math. **5**, 257 (1952).

[19] H. Grad, On the kinetic theory of rarefied gases, Commun. Pure Appl. Math. **2**, 331 (1949).

[20] H. Struchtrup and M. Torrilhon, Regularization of Grad's 13 moment equations: Derivation and linear analysis, Phys. Fluids **15**, 2668 (2003).

[21] H. Struchtrup, Heat transfer in the transition regime: Solution of boundary value problems for Grad's moment equations via kinetic schemes, Phys. Rev. E **65**, 041204 (2002).

[22] A. S. Rana, A. Mohammadzadeh, and H. Struchtrup, A numerical study of the heat transfer through a rarefied gas confined in a microcavity, Continuum Mech. Thermodyn. **27**, 433 (2015).

[23] A. Rana, M. Torrilhon, and H. Struchtrup, A robust numerical method for the R13 equations of rarefied gas dynamics: Application to lid driven cavity, J. Comput. Phys. **236**, 169 (2013).

[24] X.-J. Gu, R. Barber, B. John, and D. Emerson, Non-equilibrium effects on flow past a circular cylinder in the slip and early transition regime, J. Fluid Mech. **860**, 654 (2019).

[25] X.-J. Gu, D. R. Emerson, and G.-H. Tang, Analysis of the slip coefficient and defect velocity in the Knudsen layer of a rarefied gas using the linearized moment equations, Phys. Rev. E **81**, 016313 (2010).

[26] X.-j. Gu and D. R. Emerson, A high-order moment approach for capturing non-equilibrium phenomena in the transition regime, J. Fluid Mech. **636**, 177 (2009).

[27] X. J. Gu and D. R. Emerson, A computational strategy for the regularized 13 moment equations with enhanced wall-boundary conditions, J. Comput. Phys. **225**, 263 (2007).

[28] Z. J. Liu, C. Shu, S. Y. Chen, L. M. Yang, M. P. Wan, and W. Liu, A novel solver for simulation of flows from continuum regime to rarefied regime at moderate Knudsen number, J. Comput. Phys. **415**, 109548 (2020).

[29] Z. J. Liu, L. M. Yang, C. Shu, S. Y. Chen, M. P. Wan, W. Liu, and Z. Y. Yuan, Explicit formulations of G13-based gas kinetic flux solver (G13-GKFS) for simulation of continuum and rarefied flows, Phys. Fluids **33**, 037133 (2021).

[30] L. Mieussens, Discrete-velocity models and numerical schemes for the Boltzmann-BGK equation in plane and axisymmetric geometries, J. Comput. Phys. **162**, 429 (2000).

[31] V. Titarev, M. Dumbser, and S. Utyuzhnikov, Construction and comparison of parallel implicit kinetic solvers in three spatial dimensions, J. Comput. Phys. **256**, 17 (2014).

[32] P. Wang, M. T. Ho, L. Wu, Z. Guo, and Y. Zhang, A comparative study of discrete velocity methods for low-speed rarefied gas flows, Comput. Fluids **161**, 33 (2018).

[33] A. N. Kudryavtsev and A. A. Shershnev, A numerical method for simulation of microflows by solving directly kinetic equations with WENO schemes, J. Sci. Comput. **57**, 42 (2013).

[34] M. A. Diaz, M.-H. Chen, and J.-Y. Yang, High-order conservative asymptotic-preserving schemes for modeling rarefied gas dynamical flows with Boltzmann-BGK equation, Commun. Comput. Phys. **18**, 1012 (2015).

[35] L. M. Yang, C. Shu, W. M. Yang, Z. Chen, and H. Dong, An improved discrete velocity method (DVM) for efficient simulation of flows in all flow regimes, Phys. Fluids **30**, 062005 (2018).

[36] K. Xu and J.-C. Huang, An improved unified gas-kinetic scheme and the study of shock structures, IMA J. Appl. Math. **76**, 698 (2011).

[37] K. Xu and J.-C. Huang, A unified gas-kinetic scheme for continuum and rarefied flows, J. Comput. Phys. **229**, 7747 (2010).

[38] C. Liu, K. Xu, Q. Sun, and Q. Cai, A unified gas-kinetic scheme for continuum and rarefied flows IV: Full Boltzmann and model equations, J. Comput. Phys. **314**, 305 (2016).

[39] J.-C. Huang, K. Xu, and P. Yu, A unified gas-kinetic scheme for continuum and rarefied flows III: Microflow simulations, Commun. Comput. Phys. **14**, 1147 (2013).

[40] J.-C. Huang, K. Xu, and P. Yu, A unified gas-kinetic scheme for continuum and rarefied flows II: Multi-dimensional cases, Commun. Comput. Phys. **12**, 662 (2012).

[41] Z. Guo, R. Wang, and K. Xu, Discrete unified gas kinetic scheme for all Knudsen number flows. II. Thermal compressible case, Phys. Rev. E **91**, 033313 (2015).

[42] Z. Guo, K. Xu, and R. Wang, Discrete unified gas kinetic scheme for all Knudsen number flows: Low-speed isothermal case, Phys. Rev. E **88**, 033305 (2013).

[43] W. Weiss, Zur hierarchie der erweiterten thermodynamik, Ph.D. thesis, Technical University Berlin 1990.

[44] J. D. Au, Nichtlineare probleme und Lösungen in der erweiterten thermodynamik, Ph.D. thesis, Technical University Berlin, 2000.

[45] I. Müller and T. Ruggeri, *Rational Extended Thermodynamics* (Springer Science & Business Media, New York, 2013).

[46] H. Struchtrup, *Macroscopic Transport Equations for Rarefied Gas Flows: Approximation Methods in Kinetic Theory* (Springer, Berlin, 2005).

[47] K. H. Prendergast and K. Xu, Numerical hydrodynamics from gas-kinetic theory, J. Comput. Phys. **109**, 53 (1993).

[48] D. Chae, C. Kim, and O.-H. Rho, Development of an improved gas-kinetic BGK scheme for inviscid and viscous flows, J. Comput. Phys. **158**, 1 (2000).

[49] K. Xu, A gas-kinetic BGK scheme for the Navier–Stokes equations and its connection with artificial dissipation and Godunov method, J. Comput. Phys. **171**, 289 (2001).

[50] K. Xu and X. He, Lattice Boltzmann method and gas-kinetic BGK scheme in the low-Mach number viscous flow simulations, J. Comput. Phys. **190**, 100 (2003).

[51] G. May, B. Srinivasan, and A. Jameson, An improved gas-kinetic BGK finite-volume method for three-dimensional transonic flow, J. Comput. Phys. **220**, 856 (2007).

[52] L. M. Yang, C. Shu, J. Wu, N. Zhao, and Z. L. Lu, Circular function-based gas-kinetic scheme for simulation of inviscid compressible flows, J. Comput. Phys. **255**, 540 (2013).

[53] L. M. Yang, C. Shu, and J. Wu, A simple distribution function-based gas-kinetic scheme for simulation of viscous incompressible and compressible flows, J. Comput. Phys. **274**, 611 (2014).

[54] L. M. Yang, C. Shu, and J. Wu, A three-dimensional explicit sphere function-based gas-kinetic flux solver for simulation of inviscid compressible flows, J. Comput. Phys. **295**, 322 (2015).

[55] Y. Sun, C. Shu, C. J. Teo, Y. Wang, and L. M. Yang, Explicit formulations of gas-kinetic flux solver for simulation of incompressible and compressible viscous flows, J. Comput. Phys. **300**, 492 (2015).

[56] L. M. Yang, C. Shu, and Y. Wang, Development of a discrete gas-kinetic scheme for simulation of two-dimensional viscous incompressible and compressible flows, Phys. Rev. E **93**, 033311 (2016).

[57] Z. Y. Yuan, L. M. Yang, C. Shu, Z. J. Liu, and W. Liu, A novel gas kinetic flux solver for simulation of continuum and slip flows, Int. J. Numer. Methods Fluids **93**, 2863 (2021).

[58] Z. Y. Yuan, C. Shu, Z. J. Liu, L. M. Yang, and W. Liu, Variant of gas kinetic flux solver for flows beyond Navier-Stokes level, Phys. Rev. E **104**, 055305 (2021).

[59] P. L. Bhatnagar, E. P. Gross, and M. Krook, A model for collision processes in gases. I. Small amplitude processes in charged and neutral one-component systems, Phys. Rev. **94**, 511 (1954).

[60] K. Xu, Gas-kinetic schemes for unsteady compressible flow simulations, in *29th Annual Lecture Series Computational Fluid Dynamics, Rhode-Saint-Genese, Belgium* (1998).

[61] U. Ghia, K. N. Ghia, and C. T. Shin, High-Re solutions for incompressible flow using the Navier-Stokes equations and a multigrid method, J. Comput. Phys. **48**, 387 (1982).

[62] L. M. Yang, C. Shu, J. Wu, and Y. Wang, Comparative study of discrete velocity method and high-order lattice Boltzmann method for simulation of rarefied flows, Comput. Fluids **146**, 125 (2017).

[63] W. Yang, X.-J. Gu, D. R. Emerson, Y. Zhang, and S. Tang, Modelling thermally induced non-equilibrium gas flows by coupling kinetic and extended thermodynamic methods, Entropy **21**, 816 (2019).

[64] B. John, X.-J. Gu, and D. R. Emerson, Effects of incomplete surface accommodation on non-equilibrium heat transfer in cavity flow: A parallel DSMC study, Comput. Fluids **45**, 197 (2011).

[65] B. John, X.-J. Gu, and D. R. Emerson, Investigation of heat and mass transfer in a lid-driven cavity under nonequilibrium flow conditions, Numerical Heat Transfer, Part B: Fundamentals **58**, 287 (2010).

[66] N. D. Masters and W. Ye, Octant flux splitting information preservation DSMC method for thermally driven flows, J. Comput. Phys. **226**, 2044 (2007).

[67] L. M. Yang, C. Shu, and J. Wu, Numerical simulation of microflows by a DOM With streaming and collision processes, in *Proceedings of the ASME 5th International Conference on Micro/Nanoscale Heat and Mass Transfer* (American Society of Mechanical Engineers, 2016).

[68] S. E. Vargo, E. P. Muntz, G. R. Shiflett, and W. C. Tang, Knudsen compressor as a micro-and macroscale vacuum pump without moving parts or fluids, J. Vac. Sci. Technol. A **17**, 2308 (1999).